Acta Oceanol. Sin., 2022, Vol. 41, No. 1, P. 58–75
https://doi.org/10.1007/s13131-021-1920-1
http://www.aosocean.com
E-mail: ocean2@hyxb.org.cn

Chemical composition of sediments from the subducting Cocos Ridge segment at the Southern Central American subduction zone

Renjie Zhao[1,2], Quanshu Yan[1,2,3]*, Haitao Zhang[2,3], Yili Guan[2,3], Xuefa Shi[2,3]

[1] College of Earth Science and Engineering, Shandong University of Science and Technology, Qingdao 266590, China

[2] Key Laboratory of Marine Geology and Metallogeny, First Institute of Oceanography, Ministry of Natural Resources, Qingdao 266061, China

[3] Laboratory for Marine Geology, Pilot National Laboratory for Marine Science and Technology (Qingdao), Qingdao 266237, China

Received 24 February 2021; accepted 3 April 2021

Abstract

Subducted sediments play an important role in the magmatism at subduction zones and the formation of mantle heterogeneity, making them an important tracer for shallow crustal processes and deep mantle processes. Therefore, ascertaining the chemical compositions of different subduction end-members is a prerequisite for using subducted sediments to trace key geological processes. We reports here the comprehensive major and trace element analyses of 52 samples from two holes (U1414A and U1381C) drilled on the subducting Cocos Ridge segment at the Southern Central American (SCA) subduction zone during Integrated Ocean Drilling Program (IODP) Expedition 344. The results show that the SCA subducting sediments contain 51% (wt%) $CaCO_3$, 27% (wt%) terrigenous material, 16% (wt%) opal, and 6% (wt%) mineral-bound H_2O^+. Compared to the global trenches subducting sediment, the SCA subducting sediments are enriched in biogenic elements (Ba, Sr, and Ca), and depleted in high field strength elements (Nb, Ta, Zr, Hf, and Ti) and alkali elements (K, Rb, and Cs). Meanwhile, the sediments in this area were affected by the carbonate crash event, which could have been caused by a ~800 m rise in the carbonate compensation depth at 11 Ma in the Guatemala Basin. The reason for the sedimentary hiatus at Hole U1381C may be the closure of the Panama Isthmus and the collision between the Cocos Ridge and the Middle America Trench. In addition, the sediments from the subducting Cocos Ridge segment have influenced the petrogenesis of volcanic lavas erupted in the SCA.

Key words: subducting sediments, IODP Expedition 344, geochemistry, Southern Central American subduction zone

Citation: Zhao Renjie, Yan Quanshu, Zhang Haitao, Guan Yili, Shi Xuefa. 2022. Chemical composition of sediments from the subducting Cocos Ridge segment at the Southern Central American subduction zone. Acta Oceanologica Sinica, 41(1): 58–75, doi: 10.1007/s13131-021-1920-1

1 Introduction

The Cocos Plate is subducting beneath the Caribbean Plate along the Middle American Trench (MAT), forming an important part of the trench–arc system of the Central American subduction zone (Fig. 1a), which is an important focus area for investigations of the complex subduction processes (Carr, 1984; Carr et al., 1990, 2003; Feigenson and Carr, 1993; Hoernle et al., 2000, 2008; Saginor et al., 2013; Walker and Gazel, 2014). The subducting oceanic crusts outboard of the MAT are geochemically heterogeneous, while the subduction of oceanic crust from the Guatemala to northern Costa Rica (the Northern Central American (NCA) subduction zone (Walker and Gazel, 2014)) is associated with the formation and evolution of the East Pacific Rise, and the geochemical composition is similar to those of normal mid-ocean ridge basalts (MORB) (Carr et al., 1990; Patino et al., 2000). However, from central Costa Rica to Panama (the Southern Central American (SCA) subduction zone (Walker and Gazel, 2014)), the subducting oceanic crust is covered by the Cocos Ridge and seamount province which is the Galapagos hotspot tracks. The aseismic Cocos Ridge is subducting under southern Costa Rica while the numerous seamounts flanked northward of Cocos Ridge are subducting under central Costa Rica (Dzierma et al., 2011; Morell, 2016; Vannucchi et al., 2016). Both of these different subduction components are recognized in the lavas erupted along the strike of volcanic front (Gazel et al., 2009, 2011; Saginor et al., 2013). Therefore, the SCA subduction zone is an ideal area to study the material relationship between subduction input and arc output. A prerequisite for the subduction material cycle study is to determine the subduction input compositions and their variations along the trench (Plank and Langmuir, 1998;

Foundation item: The National Key Research and Development Program of China under contract No. 2017YFC1405502; the National Natural Science Foundation of China under contract Nos 41776070, 41322036 and 41276003; the AoShan Talents Program Supported by Pilot National Laboratory for Marine Science and Technology (Qingdao) under contract No. 2015ASTP-ES16; the Fund of Taishan Scholarship from Shandong Province.

*Corresponding author, E-mail: yanquanshu@163.com

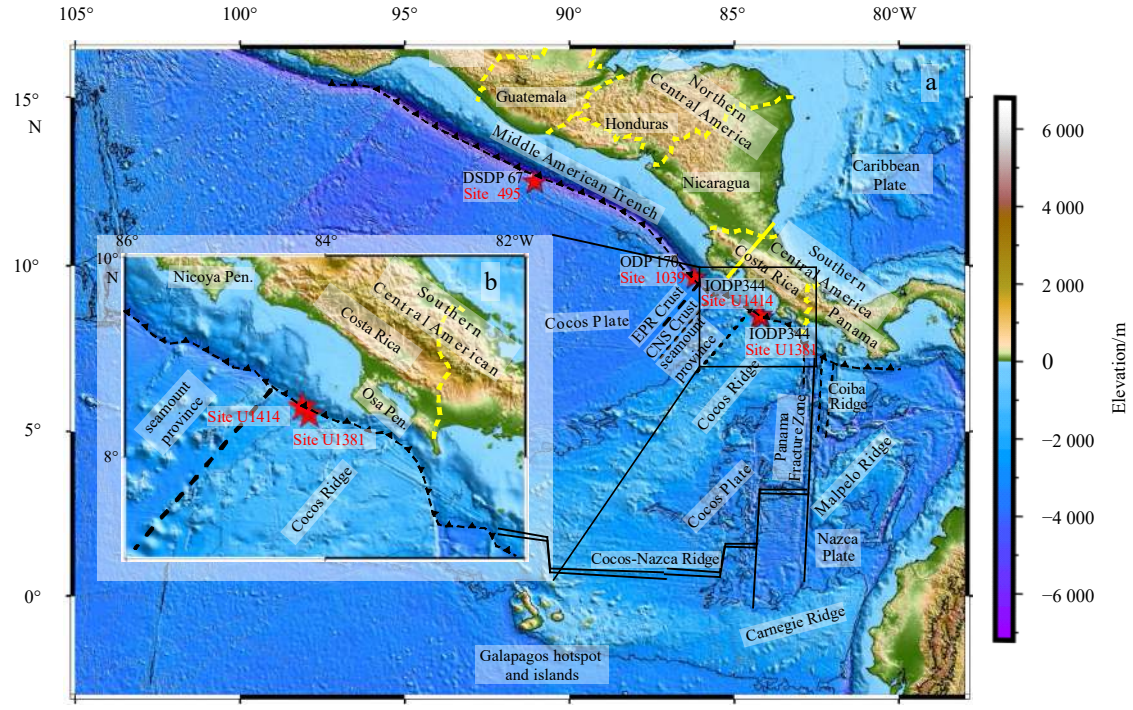

Fig. 1. Topographic map and main geologic units of the Middle American Trench (a), and the locations of Site U1381 and Site U1414 (b). The yellow solid lines are the boundary of the SCA and NCA subduction zone (Walker and Gazel, 2014), while the yellow dotted lines are the boundary of centers along strike of the Central American volcanic front (Carr, 1984). EPR represents Eastern Pacific Rise; CNS, Cocos-Nazca Spreading Center.

Plank et al., 2007; Zhao et al., 2020). Along the NCA and SCA subduction zones, the variations of composition and topography of the subducted oceanic crust are significant. For instance, the subducting crust under the NCA subduction zone is MORB-like normal oceanic crust, while the crust subducted under the SCA subduction zone including the Cocos Ridge and seamounts, which have a positive topography and have been affected by the Galapagos hotspot. However, so far, almost all the previous studies were used to choose the sediment materials from a single Deep Sea Drilling Program (DSDP) Site 495 on the Cocos Plate off Guatemala as the end-member compositions of subducting sediments for the entire MAT (Carr et al., 1990; Gazel et al., 2011; Patino et al., 2000). Therefore, thus far, a comprehensive chemical analysis data for the sediments from the subducting Cocos Ridge segment was lacking, which hinder us to understand the chemical composition characteristics of the subducting sediments at the SCA subduction zone and their impacts on the genesis of the SCA arc volcanoes.

Here we systematically analyzed major and trace elements of sediments from two holes (U1381C and U1414A) drilled during Integrated Ocean Drilling Program (IODP) Expedition 344, which are located seaward of the deformation front offshore the Osa Peninsula, SCA. They were drilled at the top and the flank of the Cocos Ridge. The bulk chemical compositions and lithological constituents of the sediments subducting at the SCA subduction zone were determined. Then, we investigated the material components of the subducting sediments at the SCA, and the differences and causes of the differences in the compositions of subducting sediments between the SCA and global trenches. Meanwhile, we discussed the reason for the sedimentary hiatus on the Cocos Ridge. Finally, we explored the possible influence of the subducting sediments on the genesis of the volcanic lavas at the SCA subduction zone.

2 Geological setting and sample descriptions

The Central American volcanic front extends for 1 100 km from Guatemala to Panama, which is the best-studied erosive subduction margin (Carr et al., 1990, 2003; Li et al., 2018; Vannucchi et al., 2006, 2013, 2016; Walker and Gazel, 2014; Yan and Shi, 2014) (Fig. 1a). Along the strike of the MAT, the convergence rates, crustal thicknesses, subduction angles, and ages of the subducting crust vary significantly. For instance, from Guatemala to Costa Rica, the convergence rate between the Cocos Plate and Caribbean Plate increases from ~60 mm/a to ~90 mm/a (DeMets, 2001). The sub-arc crustal thickness decreases from 48 km in western Guatemala to 32 km in Nicaragua, and then, it increases again to 32–40 km in Costa Rica (Carr et al., 1990). The subduction angle decreases from 65° under Nicaragua to 40° under central Costa Rica (Protti et al., 1995), while under southern Costa Rica the subduction is nearly flat. The variable ages of the subducting crust range from ~24.0 Ma for the NCA subduction zone to 13.0–14.5 Ma for the SCA subduction zone (Barckhausen et al., 2001; Werner et al., 2003). In the SCA subduction zone, the geochemical compositions of volcanic lavas from the Costa Rica have undergone obvious changes, the calc-alkaline magmatic activities shut down at ~6 Ma, while the <6 Ma lavas have the isotopic and trace element compositions with an ocean island basalt affinity, which may be caused by subduction of the Cocos Ridge and seamounts that brought the Galapagos hotspot materials into mantle wedge (Abratis and Worner, 2001; Gazel et al., 2009, 2011). Moreover, based on the isotope geochemistry and seismic velocity structure, there is trench-parallel flow in the mantle wedge beneath Costa Rica and Nicaragua (Hoernle et al., 2008).

It is generally accepted that the sediments are completely subducted at the MAT (Chan and Kastner, 2000; Patino et al.,

2000; Plank et al., 2002). Previous studies have compared the lithologic and chemical compositions of DSDP Site 495 and Ocean Drilling Program (ODP) Site 1039, and have found that the thickness and lithologic units of the sediments subducting under the NCA subduction zone are quite similar (Patino et al., 2000; Solomon et al., 2006). DSDP Site 495 is the most utilized site, which is located on a horst 22 km seaward off Guatemala. The 428 m thick sediment column overlying the basaltic oceanic crust consists of two units. The upper part of the column (177 m) consists of hemipelagic diatomaceous mud and abyssal clay, while the lower part of the column consists of chalky carbonate ooze, manganiferous chalk and chert (Aubouin and Von Huene, 1982).

To elucidate the processes controlling the nucleation and seismic rupture of large earthquakes, IODP Expeditions 334 and 344 drilled offshore Osa Peninsula of Costa Rica which obtained sediments from the subducting Cocos Ridge segment and the upper plate (Harris et al., 2013; Vannucchi et al., 2012). The Cocos Ridge is ~1 000 km long, 200–300 km wide, and about 2 km shallower than the adjacent seafloor, which is subducting under the southern Costa Rica (Ge et al., 2020; Harpp et al., 2005; Walther, 2003; Werner et al., 2003). Site U1381 (8°25.7′N, 84°9.5′W; water depth of 2 064.9 m) is located on the top of the Cocos Ridge and is ~4.5 km seaward of the deformation front offshore Osa Peninsula (Fig. 1b). Holes U1381A and U1381B were cored using the IODP rotary core barrel system, and they recovered highly disturbed sediments during the Expedition 334 (Vannucchi et al., 2012). In order to recover pristine sediment samples, Expedition 344 revisited this site and Hole U1381C was cored using the advanced piston corer system (Harris et al., 2013). Hole U1381C successfully cored about 103.83 m of sediment, sedimentary rocks, and a short interval of basaltic breccia in the lowermost part of the core. In addition, there is a sedimentary hiatus at the contact between the Unit I and Unit II (Harris et al., 2013). Site U1414 (8°30.2′N, 84°13.5′W, water depth of 2 459 m) is located on the flank of the Cocos Ridge. The drilling at Site U1414 was conducted using the advanced piston corer, extended core barrel , and rotary core barrel system, which cored about 375.25 m of sediment. Therefore, Site U1414 has a much thicker sedimentary sequence than Site U1381, and there is no sedimentary hiatus at Site U1414. The paleontology and biostratigraphy also indicate that the deposition at Hole U1414A was continuous (Harris et al., 2013). The summary of the sedimentary records from Holes U1381C and U1414A are shown in Fig. 2, and we found the lithological units between the NCA and SCA subduction zone are basically identical, but how about their chemical composition. Therefore, in this study, we selected 11 samples from Hole U1381C for geochemical analysis: 6 samples from Unit I and 5 samples from Unit II. Then we selected 41 samples from Hole U1414A, including 9 samples from Unit IA, 7 samples from Unit IB, 6 samples from Unit IIA, 13 samples from Unit IIB, and 6 samples from Unit III (Table A1).

3 Analytical methods

Because the primary goal of this study was to determine the bulk chemical compositions of the sedimentary columns being subducted under the SCA, samples were collected at evenly spaced intervals downcore, which were representative lithologies of the sediments at the two sites. The samples were freeze-dried, ground to 200 mesh, and dried again at 105°C for 3 h. Then, 0.05 g samples were digested using 3 mL of HF-HNO_3 (1:1) at 195°C for 48 h in closed Teflon beakers. The mixture was placed on a hot plate and dried under a heat lamp, and then, 1 mL of HNO_3 was added to the digested samples and evaporated to dryness. After drying, 3 mL of HNO_3 solution was added and 0.5 mL of indium was added as an internal standard. Then, the mixture was heated at 150°C for 24 h until the sample was completely digested. Finally, the digested solutions were diluted to 50 mL with Milli-Q water. The contents of the major elements, except Si, were determined using inductively coupled plasma-optical emission spectrometry at the Key Laboratory of Marine Geology and Metallogeny, Ministry of Natural Resources, China. The SiO_2 contents of the samples were analyzed using X-ray fluorescence at the Forth Exploration Institute of Geology and Mineral Resources of Shandong Province, China. The contents of the trace elements were measured using the inductively coupled plasma-mass spectrometer at the Key Laboratory of Marine Geology and Metallogeny, Ministry of Natural Resources, China. The precisions are (±0.2%)–(±2%) for major elements at contents >1% (wt%) (Al_2O_3, MgO, CaO, and TFe_2O_3), and about (±2%)–(±5%) for minor elements at contents <1.0% (wt%) (TiO_2, MnO, Na_2O, K_2O, and P_2O_5). The precision of the trace elements is within 10%. The loss on ignition was also measured. The accuracy was checked by measuring United States Geological Survey chemical reference standard BHVO-2 with every batch of unknowns. The measured value is consistent with the recommended value within the error range (Table A1).

4 Results

4.1 *Age model and sedimentation rates of Holes U1381C and U1414A*

The age model for Holes U1381C and U1414A is from the results of Maria et al. (2017), and it is based on shipboard nannofossil data (Harris et al., 2013), the $^{40}Ar/^{39}Ar$ ages of tephra (Schindlbeck et al., 2015), tephra correlations (Schindlbeck et al., 2016a, b), and post-shipboard paleomagnetic analyses (Li et al., 2015) (Fig. 3a). The mean sedimentation rate was ~80 m/Ma for the first 0.6 Ma in Hole U1381C, and then, it decreased to ~10 m/Ma at the Unit I/II boundary (middle late Miocene). The sedimentation rate for the Unit II was generally within the range of open-ocean, deep sea marine sediments (~5 m/Ma). At Hole U1414A, the sedimentation rate was ~150 m/Ma for the first 0.6 Ma, and then it steadily decreased to ~9 m/Ma at the Unit IIA/IIB boundary. Then, at the late Miocene, the sedimentation rate increased to ~35 m/Ma (Fig. 3b).

4.2 *Geochemical variations in subducted sediments at the SCA*

There are large geochemical variations in Holes U1381C and U1414A from the bottom to the top (Fig. 4). In Hole U1414A, the variation trends of $CaCO_3$, CaO, and Sr abundances are similar. Their abundances are high in the Unit III and Unit IIB except that significant abrupt decrease fluctuation in the 11–9 Ma internal. In Units IIA and IB, their abundances gradually decreases. In Unit IA, the change is relatively large due to the high variation of the loss on ignition. In Fig. 4, the change in SiO_2, Al_2O_3, K_2O, and Th contents are similar, but are opposite to the change in CaO content. Compared with Sr, the abundance of Ba fluctuated more obviously. From the bottom to about 10 Ma, the Ba content gradually increases, and then, it decreases until 8 Ma. In the 8–6 Ma interval, the Ba content abruptly increases to a high value and then decreases to a lower value. In the rest of units, the abundance of Ba fluctuates at relatively low levels. Because of the sedimentary hiatus at Hole U1381C (Harris et al., 2013; Li et al., 2015), it is hard to constrain the geochemical variations in the sediments. However, as can be seen from Fig. 4, the Unit II of Hole U1381C is enriched in $CaCO_3$, CaO, and Sr, but the Al_2O_3, K_2O, and Th contents are low. In Unit I, the trends of these elements are reversed.

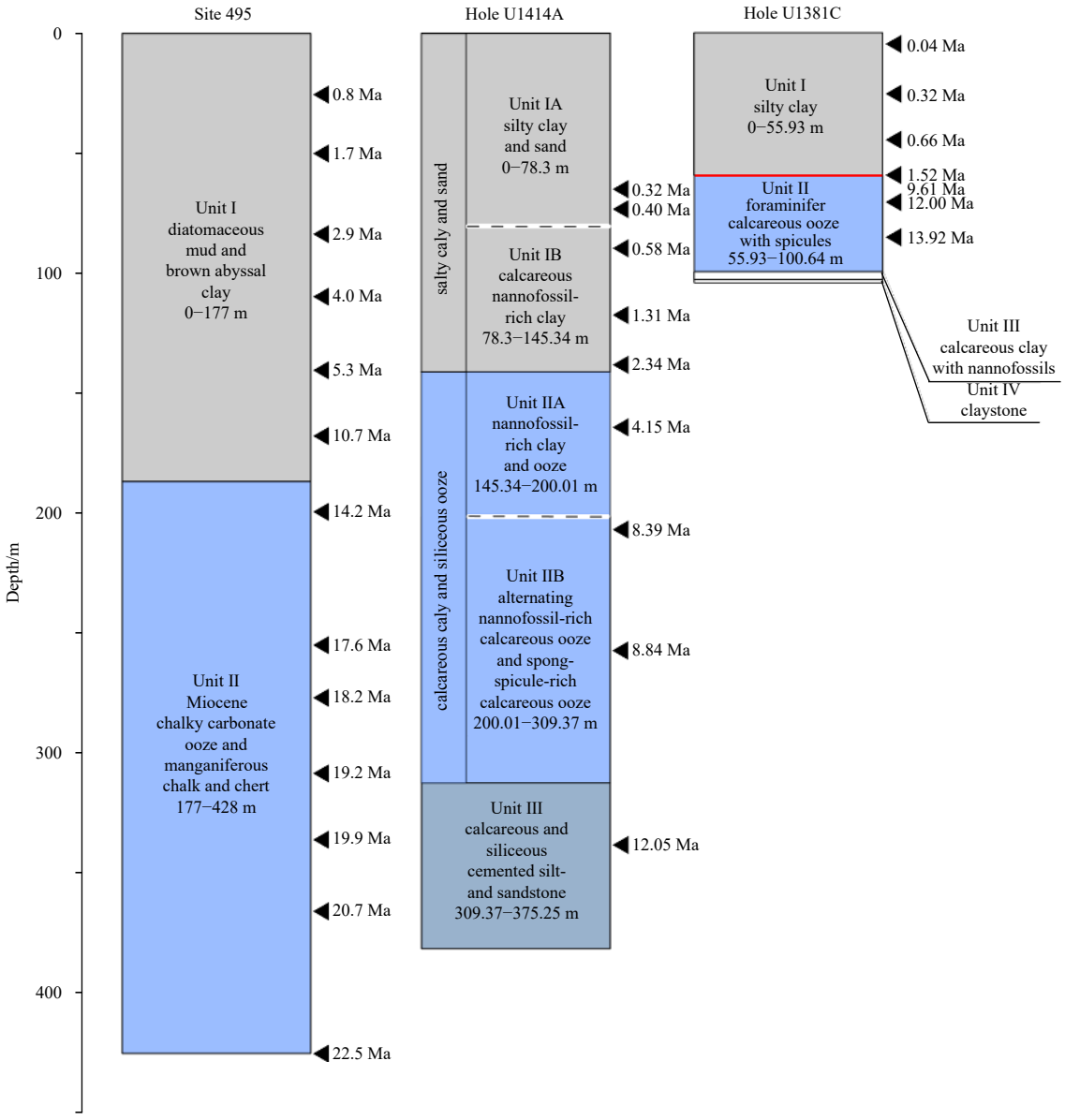

Fig. 2. Sedimentary records from DSDP Site 495, IODP Hole U1414A and IODP Hole U1381C. The red line is the sedimentary hiatus at Hole U1381C. The lithostratigraphy and age data for Holes U1414A and U1381C are from Harris et al. (2013) and Sandoval et al. (2017). The lithostratigraphy and age data for Site 495 are from Patino et al. (2000). And there is only one hole at the Site 495 (Aubouin and Von Huene, 1982).

In contrast to Hole U1414A, the SiO_2 content in Unit II of Hole U1381C is high, and the Ba content essentially remains unchanged.

4.3 *Calculating the bulk composition of each site*

Plank et al. (2007) compared the core analyses and the logging data from ODP Site 1149, and they concluded the deviation between the two methods was <20% when the sedimentary column had a high recovery. Therefore, the bulk composition of two sites can be calculated using the core analyses, due to the recoveries of Holes U1381C and U1414A are 105% and 84%, respectively (Harris et al., 2013; Plank and Langmuir, 1998). First, the sedimentary column was broken into several lithological units. Second, we analyzed the major and trace elements of several samples from each lithological units, and we used the average value as the bulk composition for each units. Finally, the bulk compositions of two sites can be calculated from the chemical compositions and mass proportions of the each unit of site, where the mass proportions are the product of the dry bulk density and the length of the core (Plank and Langmuir, 1998; Plank et al., 2007). The bulk composition for Hole U1381C (Tables A2 and A3) is based on 11 analyses with complete major and trace element, and that of Hole U1414A (Tables A2 and A3) is based on the 41 analyses. The relative standard deviation of each unit was based on core analyses of each unit, while the relative standard deviation of bulk composition was based on each analyse of the site.

Based on the bulk composition calculations, we further normalized the elemental compositions to the average upper continental crust (UCC) and compared them with the subducting sediment compositions of each trench. Based on the data from Plank and Langmuir (1998) and Plank (2014), we further divided the

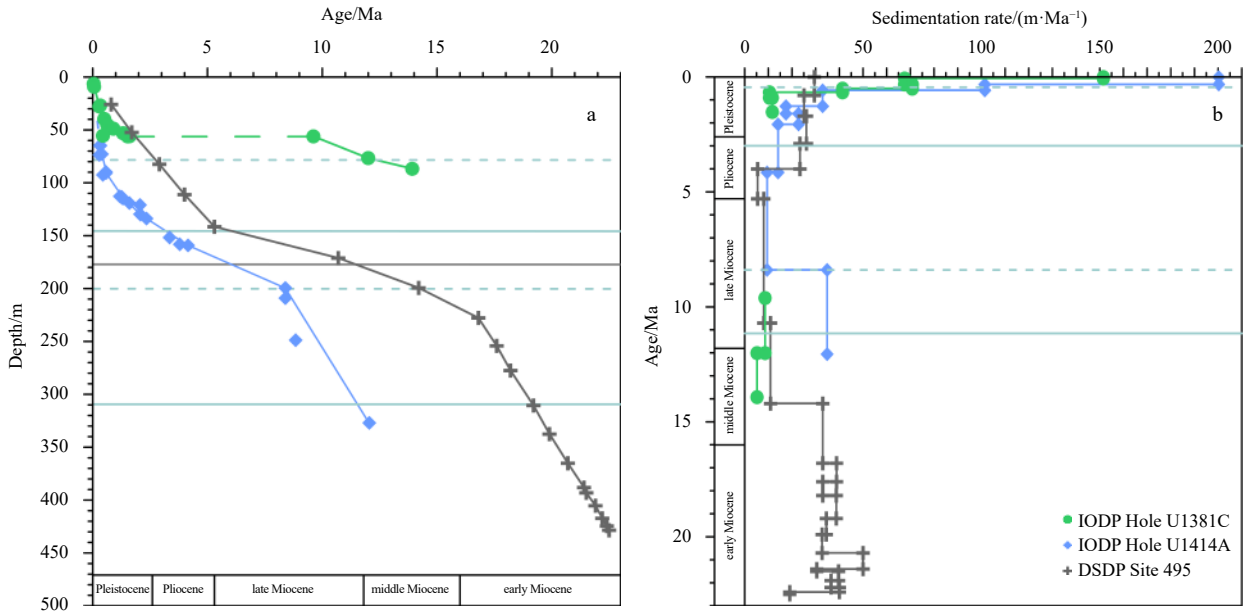

Fig. 3. Age model (a) and sedimentation rate (b). The green dash line represents the sedimentary hiatus. The light-blue solid lines are the lithological boundaries of Hole U1414A, and the light-blue dotted horizontal lines are the subunit boundaries of Hole U1414A (Harris et al., 2013). The gray solid line is the lithology boundary of Site 495 (Aubouin and von Huene, 1982). The data for Holes U1381C and U1414A are from Sandoval et al. (2017), while the data for Site 495 are from Patino et al. (2000).

global subducting sediment into accretionary margin and nonaccretionary (erosion) margin subducting sediment (Fig. 5).

5 Discussion

5.1 *Material components of the sediments subducting in the SCA*

According to the core length, plate motion vectors, and the paleolatitude, during the late Miocene, Holes U1381C and U1414A were located close to the Galapagos hotspot, near the equator (Sandoval et al., 2017). But now, they are located near the trench in the low latitudes of the SCA. Therefore, the sedimentary environments and material components of Holes U1381C and U1414A might have changed significantly. Owing to the geochemical variations could be on the centimeter scale at sediment column, and the sample intervals of Holes U1381C and U1414A were about 10 m (as in the study of Plank et al. (2007)), the detailed interpretations for the sedimentation processes are not the scope of this study. Therefore, we discuss the material components of the two sites.

The global subducting sediment consists of 76% (wt%) terrigenous material, 7% (wt%) calcium carbonate, 10% (wt%) opal, and 7% (wt%) mineral-bound H_2O^+ , which means the global subducting sediment is dominated by the terrigenous and biogenic components (Plank and Langmuir, 1998; Plank, 2014). Therefore, we selected several terrigenous and biogenic elements to represent the material components of the SCA subducting sediments. The CaO and SiO_2 contents of the sediments are influenced by terrigenous and biogenic phases, while the K_2O, Al_2O_3 and Th content are strongly linked to terrigenous material and the extent of dilution by biogenic phases (Plank and Langmuir, 1998; Plank, 2014). Ba and Sr are strongly linked to biogenic phases and biological productivity, and in marine sediments, Sr can substitute for Ca in calcium carbonate.

There is sedimentary hiatus at the Hole U1381C, thus we only discuss the geochemical temporal variability of Hole U1414A. From bottom to top, we found that the $CaCO_3$, CaO, and Sr contents decrease in Unit IIA of Hole U1414A (~8 Ma), while K_2O, Al_2O_3, and SiO_2 contents increase. And the $CaCO_3$, CaO, and Sr content are mainly high in Units IIB and III, but they exhibit a decreasing fluctuation in Unit IIB (Fig. 4). However, the $CaCO_3$ and CaO variations are not synchronous as a result of the analytical methods. The $CaCO_3$ content was calculated from the total inorganic carbon content that assuming all evolved CO_2 was derived from the dissolution of $CaCO_3$, but a correction was not made for the presence of other carbonate minerals (Harris et al., 2013). Therefore, the CaO content may represent the preservation of carbonate in Hole U1414A. According to the carbonate variations at Site 495, there was a drastic decrease in $CaCO_3$ at ~11 Ma, which was largely synchronous with the carbonate crash (Plank et al., 2002). The carbonate crash event was caused by the closure of the Central American seaway, and it lifted the carbonate compensation depth by about 800 m, which apparently prevented the flow of less corrosive Caribbean intermediate and deeper water into Pacific (Lyle et al., 1995; Newkirk and Martin, 2009). Therefore, the CaO content of Hole U1414A may also have been influenced by the crash event, even though the depth is shallower than the carbonate compensation depth (Lyle et al., 1995).

By comparing the contents of key elements in Holes U1381C and U1414A (Fig. 6), we found that K_2O is positively correlated with Al_2O_3 and SiO_2, but it is negatively correlated with Sr. This indicates that the sediments from subducting Cocos Ridge segment at the SCA are composed of biogenic material and terrigenous material. In Fig. 4, the terrigenous material content increases in Unit IIA of Hole U1414A, while the bottom units (Unit IIB and III) of Hole U1414A have high contents of biogenic elements. This suggests that the top units (Units IA, IB and IIA) are mostly dominated by terrigenous materials, the content of which increased in the late Miocene (~8 Ma), while the underlying units mainly consisted of biogenic phases (Plank and Langmuir, 1998; Plank, 2014). In the bottom units, the CaO and Sr contents are positively correlated, while SiO_2 and CaO contents are not significantly correlated with Ba content. This indicates that the bio-

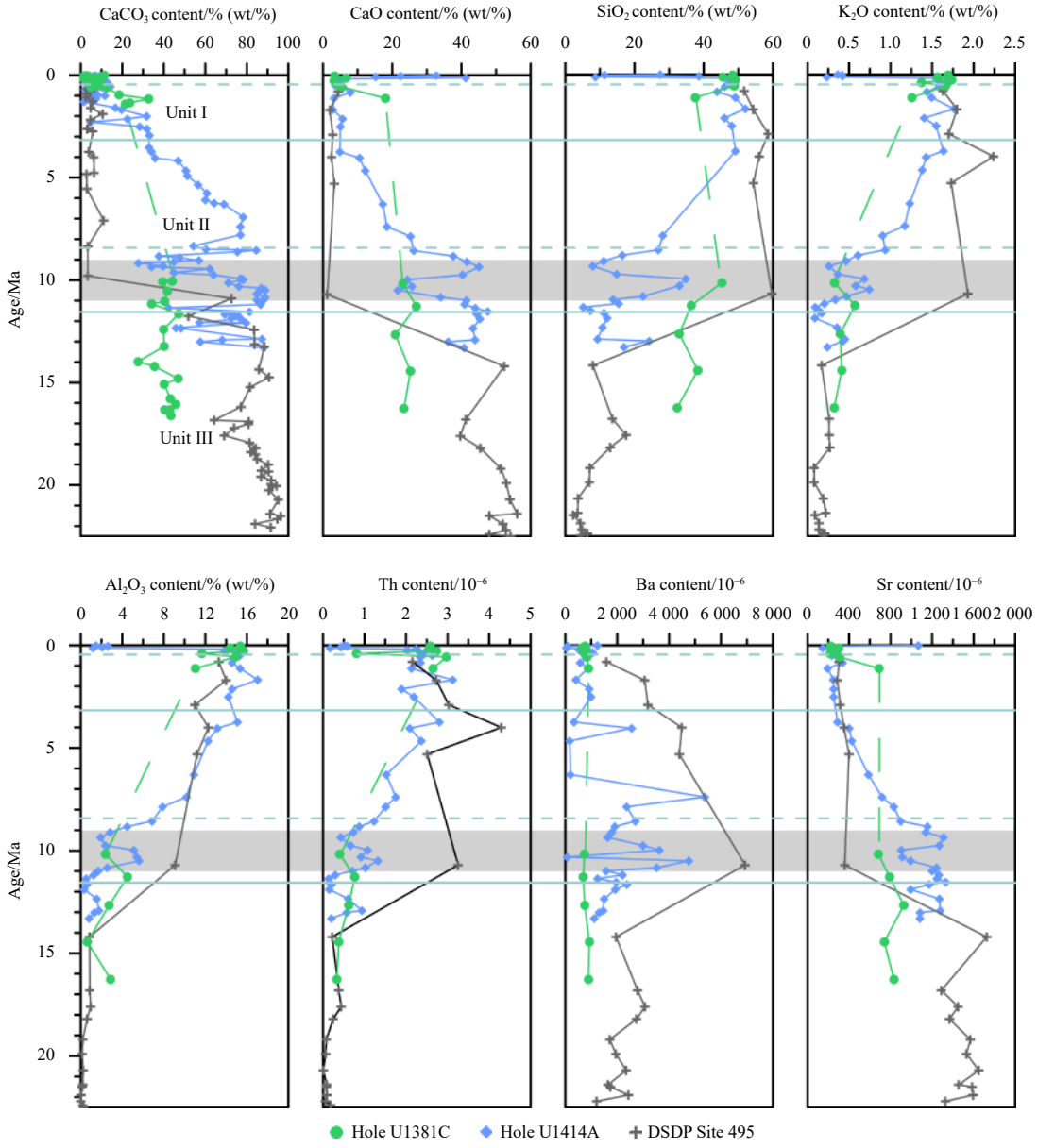

Fig. 4. The geochemical variations in Hole U1381C, Hole U1414A, and DSDP Site 495. Grey shades area is the 11–9 Ma carbonate crash event in the Guatemala Basin (Lyle et al., 1995). The light-blue solid lines are the lithological boundaries of Hole U1414A, and the light-blue dotted lines are the subunit boundaries of Hole U1414A (Harris et al., 2013). Note that the lithological boundary between the hemipelagic sediments (Unit I) and carbonate sediments (Unit II) in Site 495 is contemporary with the boundary between Unit IIB and Unit III in Hole U1414A. The lithological boundary of Hole U1381C is the sedimentary hiatus. The $CaCO_3$ data for Hole U1381C and Hole U1414A are from Harris et al. (2013), and the geochemical data for Site 495 are from Plank et al. (2002).

genic phases consisted of both the siliceous and calcareous materials. As can be seen from Fig. 6, the compositions of the top units of Holes U1381C and U1414A are closest to the composition of UCC and accretionary margins. Given the geographic positions of the holes, the terrigenous source should have been either from the Central American volcanic arc or from the Galapagos hotspot. Therefore, we selected the lavas from Costa Rica to represent the terrigenous component, while chose the compositions of basaltic rocks from Cocos Ridge and seamount province to represent the hotspot component as these rocks were formed by Galapagos hotspot (Harpp et al., 2005; Walther, 2003; Werner et al., 2003). The rare earth element (REE) (Fig. 7) compositions suggest that the terrigenous source is the Oligocene–middle Miocene lavas in Costa Rica (Schindlbeck et al., 2015). This means that the terrigenous material may be from the South American and/or North American continents.

5.2 *Comparison of the SCA bulk sediments to other sediment averages*

It is useful to compare the bulk sediment compositions of the SCA with the bulk sediment compositions of the NCA (Plank named the bulk sediments of the Central America Trench) and global subducting sediment (GLOSS-II) (Plank, 2014).

The NCA subducting sediments are mostly based on Site 495 with some tracer elements (U, Th, Pb, REE, Nb, Hf, and Ta) from the ODP Sites 844 and 845 (Plank, 2014). Figure 5 shows that the sediments of the SCA are enriched in high field strength elements (HFSE: Nb, Ta, Zr, Hf, and Ti) and U, and are depleted in biogenic elements and Mn relative to the sediments from the

NCA. Because the content of the HFSE is linked to terrigenous material, while the extent of dilution by biogenic phases, and the content of U is related to the redox state of the depositional environment (Plank and Langmuir, 1998; Plank, 2014). Therefore, the SCA sediments contained more terrigenous material and were deposited in an oxygenated environment, which may be due to the positive topography. Then the enrichment of Mn in the NCA sediments is due to the manganiferous clay within the carbonate unit (Aubouin and Von Huene, 1982). Thus, the diffences in subducted sediments between the SCA and NCA could be attributed to the different sedimentary environments. The GLOSS-II is similar to the UCC, which is mainly controlled by terrigenous materials (Plank and Langmuir, 1998; Plank, 2014). In Fig. 5, we found that nonaccretionary margin subducting sediment is depleted in alkaline elements and HFSEs, which may be due to the nonaccretionary margin is far from the continent (Plank and Langmuir, 1998; Zhao et al., 2020). As a typical nonaccretionary margin, the subducted sediments of the SCA also have less content of terrigenous material, which may be due to the SCA trench is located at low latitudes where the seafloor is overlain by regions of high biological productivity (Schindlbeck et al., 2016a). Therefore, in contrast to other subduction zones, the SCA subduction zone subducts substantial sedimentary carbon (Plank and Manning, 2019). This observation is consistent with quantitative estimates of the proportion of calcium carbonate, opal and terrigenous materials (Table 1). The opal and $CaCO_3$ contents are from shipboard analyses (Harris et al., 2013). Thus, the sediments in Hole U1414A contain 51% (wt%) $CaCO_3$, 27% (wt%) terrigenous material, 16% (wt%) opal, and 6% (wt%) mineral-bound H_2O^+.

In conclusion, the subducted crust with positive topography makes the chemical compositions of subducted sediments different, although they were located at the same trench. Thus, in the study of re-circulation of material at subduction zone, we should select the appropriate end-member of subducted sediments.

5.3 *Origin of the sedimentary hiatus*

Previous studies have concluded that the sedimentary hiatus does not occur everywhere on the Cocos Plate, but rather it appears to be restricted to the top of the Cocos Ridge and near the MAT (Li et al., 2015; Schindlbeck et al., 2016a). However, the reasons for the formation of this hiatus are on debate. Li et al. (2015) suggested that the hiatus may be the result of the collision between the Cocos Ridge and the MAT, which resulted in bottom current erosion or Cocos Ridge buckling. In Fig. 3, we found that the sedimentation rate of Hole U1414A increased since ~1.3 Ma, the increased sediments could be the erosional material from Hole U1381C, which was caused by the subduction of the topographic relief (Li et al., 2015). However, we found that the sedimention rate of Hole U1414A also increased at ~4 Ma, which was contemporary with the closure of Panama Isthmus (Reijmer et al., 2002; Stone, 2013). So some researchers proposed that the closure of Panama Isthmus caused the strong bottom currents, which could explain the sedimentary hiatus in top of positive topography (Sandoval et al., 2017; Schindlbeck et al., 2016a). As mentioned above, both of above events influenced the sedimentation processes at Holes U1381C and U1414A, they brought the sediment components from Hole U1381C to Hole U1414A. Therefore, both the closure of the Panama Isthmus and the collision between the Cocos Ridge and the MAT could have caused the sedimentary hiatus on the top of the Cocos Ridge.

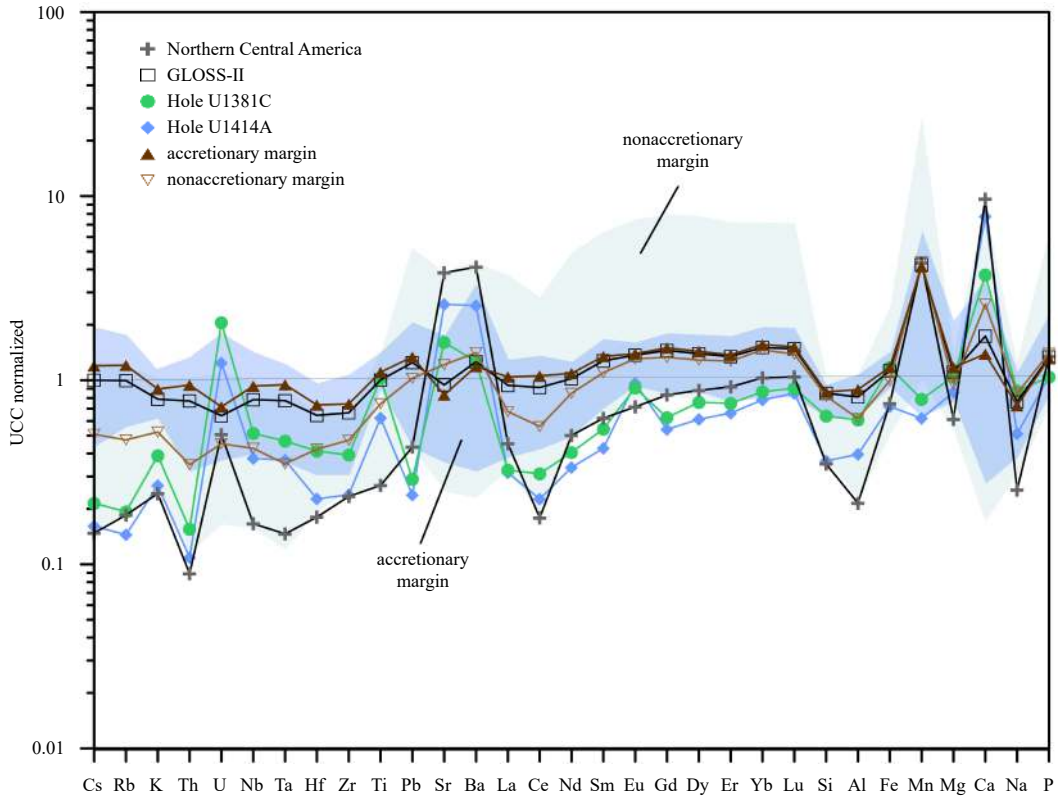

Fig. 5. The elemental compositions of the subducting sediment of the global trenches normalized to the the average upper continental crust (UCC). The global subducting sediment (GLOSS-II) data are from Plank (2014); the UCC data are from Rudnick and Gao (2014).

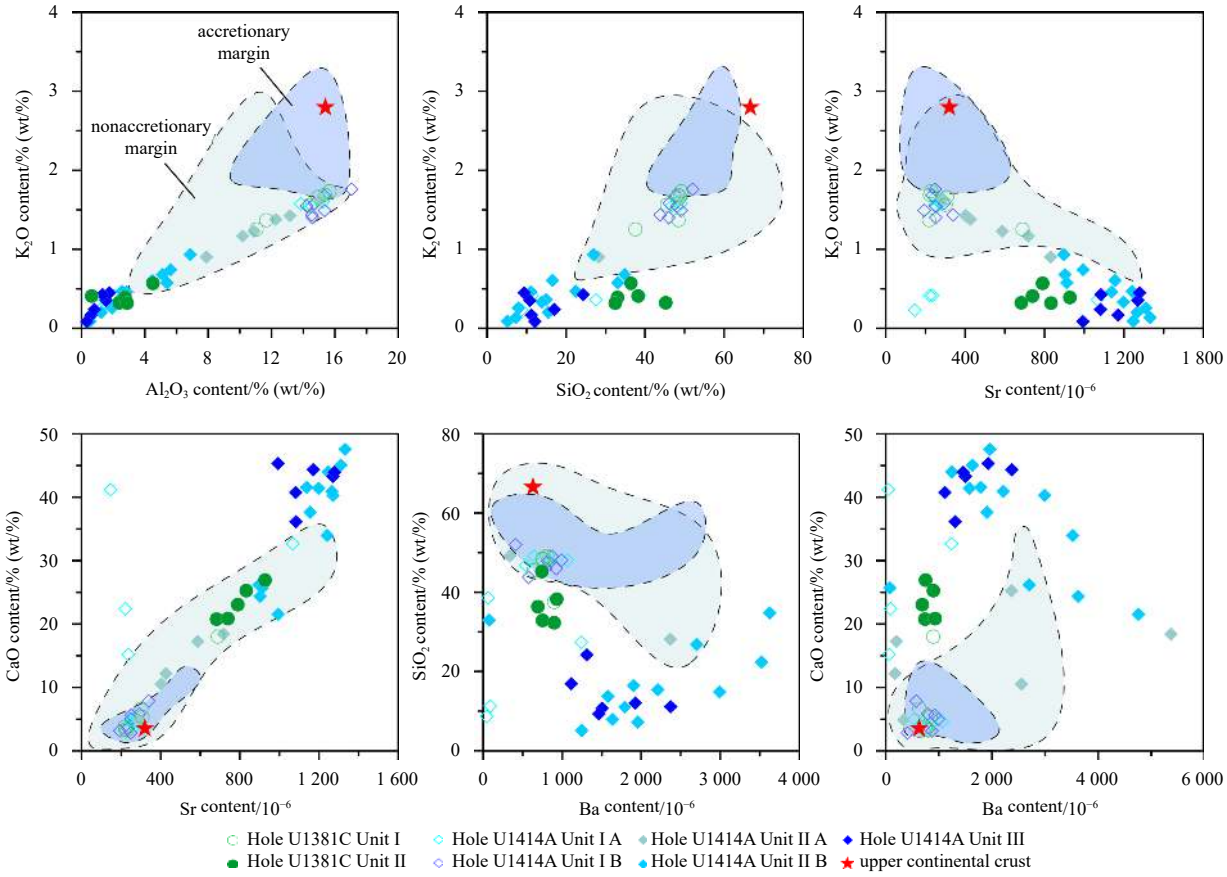

Fig. 6. Comparision of the contents of key elements in Holes U1381C and U1414A. The data for accretionary margins and nonaccretionary margins are from Plank (2014). The average upper continental crust data are from Rudnick and Gao (2014).

5.4 *Using the SCA sediments to address subduction recycling*

We used the bulk composition of the SCA sediments presented here to investigate the origin of the SCA arc lavas. During subduction, the subducted sediments released fluids, melts, and/or supercritical fluids, which were incorporated into the arc magma source and influenced the geochemical compositions of the arc lavas (Plank, 2014; Spandler and Pirard, 2013; Zhao et al., 2020). Elements such as large ion lithophile elements (Rb, Sr, Ba and Cs), B, and Pb migrate with the subduction fluids, while Th and the light REEs (LREEs) only migrate with the melts (Johnson and Plank, 2000; Yan et al., 2019). Therefore, Th and the LREEs are mainly derived from the mantle source and subducted melts. The HFSEs and high rare earth elements can be regarded as subduction immobile elements, so the ratios of subduction mobile to subduction immobile elements can be used to identify the subducbtion components (Pearce et al., 2005; Pearce and Stern, 2006; Yan et al., 2019; Zhang et al., 2019). To eliminate the influence of fractional crystallization, we used Pb/Ce and Ba/Th content ratios to identify the hydrous fluids, Th/Nb and Th/La content ratios to identify the subduction melts, and Ba/Nb content ratio to calculate the amount of subduction materials added to the mantle source (Pearce et al., 2005; Pearce and Stern, 2006; Plank, 2005; Yan et al., 2019).

We compiled subduction input and arc output data to investigate the subduction recycling process, and the most striking feature of the output lavas from the SCA is that the relatively recent origin (late Miocene, ~6 Ma) lavas have similar isotopic and trace element compositions to the Galapagos-OIB lavas (Gazel et al., 2009, 2011). Therefore, previous studies have presented several models to explain these geochemical characteristics. Abratis and Woner (2001) suggested that there is a slab window in the subducting Cocos Plate, which allows the OIB-type asthenosphere mantle into the mantle wedge under the SCA. Feigenson et al. (2004) proposed that the OIB signature is from residual Galapagos component after the formation of the Caribbean Large Igneous Province (CLIP). Goss and Kay (2006) explained the OIB signature by subduction erosion, which carried the accreted Galapagos material (upper plate basement) into the mantle wedge. Gazel et al. (2011) suggested that slab detachment allowed the hotter asthenosphere flow into the mantle wedge. This could explain the OIB signature as a result of mixture between mantle melts and slab melts from the subducting Galapagos tracks (Cocos Ridge and seamount province). However, the Tl and Be isotopes for arc lavas from Costa Rica have revealed either attenuated or limited evidence of the presence of sediments in their mantle source regions (Nielsen et al., 2017; Tera et al., 1986). In this study, we discuss whether the sediments from subducting Cocos Ridge segment have influenced the SCA arc lavas. Therefore, we compiled data for all of the subduction components, including subducted sediments, rocks from Galapagos tracks (Cocos Ridge and seamount province), and upper plate basement materials. Owing to the fact that basement rocks have not been obtained from the sites on the upper plate, we chose the coarse grain sizes from bottom units of the upper plate sites and the Costa Rica fore-arc CLIP oceanic complexes to represent the basement of the upper plate (Gazel et al., 2009; Straub et al., 2015). In Fig. 8, the high Pb/Ce, Ba/Th, and Ba/Nb content ratios of arc lavas could be derived from the subducted sediments, be-

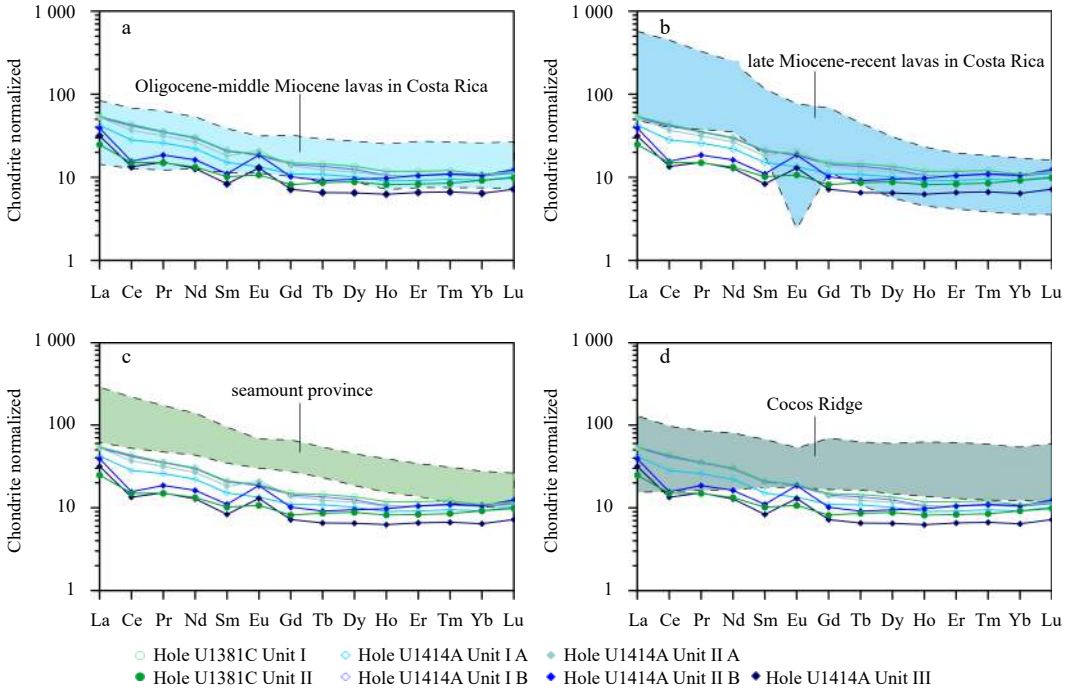

Fig. 7. The rare earth element (REE) patterns of each unit in Holes U1381C and U1414A normalized to the chondrite. The data for chondrite is from Sun and McDonough (1989). a. The shaded region represents the Oligocene–middle Miocene lavas in Costa Rica, and the data are from Gazel et al. (2009, 2011); b. the shaded region represents the late Miocene–recent lavas in Costa Rica, and the data are from Gazel et al. (2009, 2011); c. the shaded region represents the seamounts, and the data are from Harpp et al. (2005), Hoernle et al. (2000), and Werner et al. (2003); d. the shaded region represents the lavas from Cocos Ridge, and the data are from Harpp et al. (2005); Hoernle et al. (2000), Werner et al. (2003), and Yan and Shi (2014).

cause the subducted sediments show higher Pb/Ce, Ba/Th, and Ba/Nb content ratios than arc lavas among the subduction end-members. It may indicate that these geochemical variations could contribute to the mixing of depleted MORB mantle (DMM) and subducted sediments (Figs 8a and b). Meanwhile, some <6 Ma lavas with lower Pb/Ce content ratio than DMM were influenced by the Cocos Ridge and/or upper plate components, which was caused by the change of subduction style as the model proposed by the Gazel et al. (2011) or Goss and Kay (2006). We could not determine which model is right from graphs of element ratios, which needs some more work to addressed in the future. Besides, Th/Nb and Th/La content ratios could indicate sediments melt (Pearce et al., 2005; Plank, 2005; Yan et al., 2019), so the subducted sediments influenced the arc lavas in the form of melts (Figs 8c and d). It should be noted that the arc lavas have higher Th/Nb content ratios than that in the subduction components, which may be due to the variational degree of melting and fractional crystallization. We cannot quantify the addition of subducted sediments added to the arc magmas, which requires a combination of various indicators (radioactive isotopes and stable isotopes) and geophysical methods to limit the influence of each subduction component to the arc lavas of the SCA. It is worth noting that the NCA subducted sediments may have also influenced the genesis of the SCA arc lavas as shown in Fig. 8. However, as mentioned above, there are some geochemical differences between the NCA and SCA subducted sediments as the different sedimentary environment, which would not cause the obvious difference in elements ratios. Therefore, the appropriate end-member of subducted sediments is important for the subduction recycling process.

Table 1. The lithological parameters of each sub-unit of Hole U1414A

	Unit IA	Unit IB	Unit IIA	Unit IIB	Unit III	Bulk
Thickness/m	78.30	67.04	54.67	109.36	65.88	375.25
Wet bulk density/ ($g \cdot cm^{-3}$)	1.45	1.51	1.68	1.62	1.93	1.63
Water content/%	74	71	61	63	44	63
Dry bulk density/ ($g \cdot cm^{-3}$)	0.38	0.44	0.66	0.60	1.09	0.62
Mass proportion/%	13	13	16	28	31	100
$CaCO_3$ content/%	5	13	57	67	69	51
Opal content/%	1	1	1	27	24	16
Mineral-bound H_2O^+ content/%	19	7	0	4	6	6
Terrigenous content/%	75	79	42	1	1	27

6 Conclusions

In this study, we analyzed 52 samples of two holes (U1381C and U1414A) from the IODP Expedition 344, which are located on the subducting Cocos Ridge segment at the SCA subduction zone. Based on the results, we have reached the following conclusions.

The thicknesses and sedimentation rates of the two sites are different, but they have similar chemical compositions and lithologic units. The sediments subducting at the SCA have been the least affected by the terrigenous material, and they contain 51% (wt%) $CaCO_3$, 27% (wt%) terrigenous material, 16% (wt%) opal, and 6% (wt%) mineral-bound H_2O^+.

The bottom units of the SCA sediments mainly consist of biogenic phases, while the top units are dominated by terrigenous

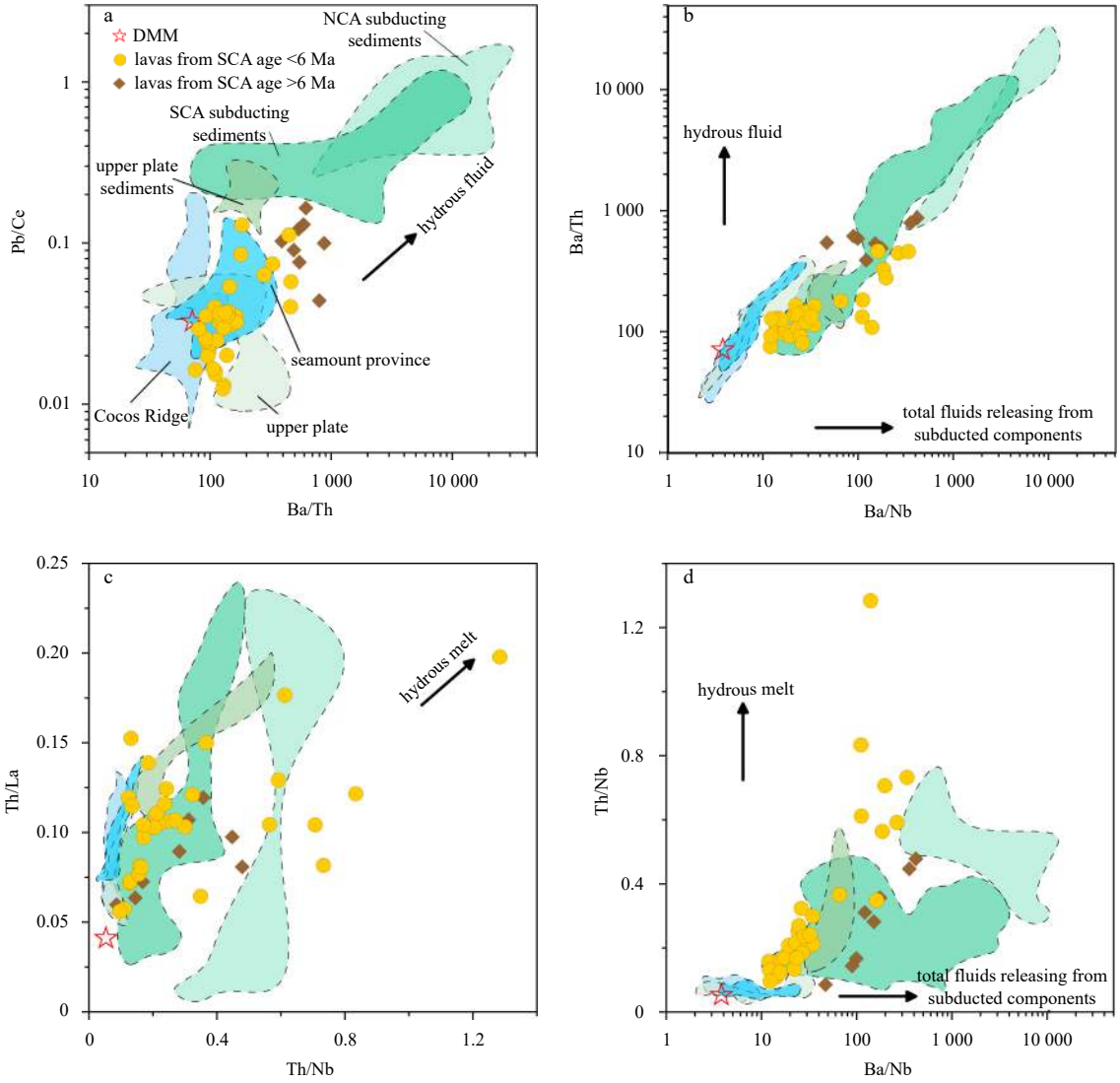

Fig. 8. Plots of the content ratios of Pb/Ce versus Ba/Th (a); the content ratios of Ba/Th versus Ba/Nb (b); the content ratios of Th/La versus Th/Nb (c); and the content ratios of Th/Nb versus Ba/Nb (d). The data for the Cocos Ridge and seamounts are from Harpp et al. (2005), Hoernle et al. (2000), Werner et al. (2003), and Yan and Shi. (2014), and the data for the SCA lavas are from Gazel et al. (2009, 2011). To eliminate the effect of fractional crystallization and assimilation, we selected the arc lavas with MgO content >6.0% (wt%). The data for upper plate are from Hoernle er al. (2000), while the data for upper plate sediments are from Zhao et al. (2021), and the data for depleted mid-ocean ridge basalts mantle (DMM) are from Workman and Hart (2005).

material, which increased in the late Miocene. The terrigenous material may be from the South American and/or North American continents. Owing to the differences in the sources of terrigenous materials and the manganiferous clay, the chemical compositions of the SCA and NCA subducting sediments have distinct HFSE and Mn contents, while the other elements have similar variation trends. Compared with other global trench subducting sediment, the sediments subducting at the SCA are enriched in biogenic elements (Ba, Sr, and Ca) and are depleted in HSFEs (Nb, Ta, Zr, Hf, and Ti) and alkali elements (K, Rb, and Cs). And in contrast to other subduction zones, the SCA subducted sediments contained substantial sedimentary carbon. Therefore, we should select the appropriate end-members of subducted sediments, as the chemical compositions of subducted sediments would be different at same trench.

In addition, the reason for the hiatus at the top of the Cocos Ridge, which is near the trench, may be the closure of the Panama Isthmus and/or collision between the Cocos Ridge and the MAT. The sediments from subducting Cocos Ridge have an effect on the arc magmas of the SCA. In future research, we need to combine various indicators to determine the influence of subducted sediments to the arc magmatism in an erosive convergent margin.

Acknowledgements

We are grateful to the crew and technical staff of the *JOIDES Resolution* for their hard work during IODP Expedition 344, and IODP-China. We thank three anonymous reviewers for their constructive comments and suggestion, and Lin'ao Zhou for editorial handling. We thank LetPub (www.letpub.com) for its linguistic assistance during the preparation of this manuscript.

References

Abratis M, Worner G. 2001. Ridge collision, slab–window formation,

and the flux of Pacific asthenosphere into the Caribbean realm. Geology, 29(2): 127–130, doi: 10.1130/0091-7613(2001)029<0127:RCSWFA>2.0.CO;2

Aubouin J, Von Huene R. 1982. Initial Reports of the Deep Sea Drilling Project, Volume 67. Washington, D. C. : U. S. Government Printing Office, 799

Barckhausen U, Ranero C R, Von Huene R, et al. 2001. Revised tectonic boundaries in the Cocos Plate off Costa Rica: Implications for the segmentation of the convergent margin and for plate tectonic models. Journal of Geophysical Research: Solid Earth, 106(B9): 19207–19220, doi: 10.1029/2001JB000238

Carr M J. 1984. Symmetrical and segmented variation of physical and geochemical characteristics of the Central American volcanic front. Journal of Volcanology and Geothermal Research, 20(3–4): 231–252, doi: 10.1016/0377-0273(84)90041-6

Carr M J, Feigenson M D, Bennett E A. 1990. Incompatible element and isotopic evidence for tectonic control of source mixing and melt extraction along the Central American arc. Contributions to Mineralogy and Petrology, 105(4): 369–380, doi: 10.1007/BF00286825

Carr M J, Feigenson M D, Patino L C, et al. 2003. Volcanism and geochemistry in Central America: progress and problems. In: Eiler J M, ed. Inside the Subduction Factory, Geophysical Monograph Series. Washington, D. C: AGU, 153–174

Chan L H, Kastner M. 2000. Lithium isotopic compositions of pore fluids and sediments in the Costa Rica subduction zone: implications for fluid processes and sediment contribution to the arc volcanoes. Earth and Planetary Science Letters, 183(1–2): 275–290, doi: 10.1016/S0012-821X(00)00275-2

DeMets C. 2001. A new estimate for present-day Cocos-Caribbean Plate motion: Implications for slip along the Central American volcanic arc. Geophysical Research Letters, 28(21): 4043–4046, doi: 10.1029/2001GL013518

Dzierma Y, Rabbel W, Thorwart M M, et al. 2011. The steeply subducting edge of the Cocos Ridge: Evidence from receiver functions beneath the northern Talamanca Range, south-central Costa Rica. Geochemistry, Geophysics, Geosystems, 12(4): Q04S30, doi: 10.1029/2010GC003477

Feigenson M D, Carr M J. 1993. The source of Central American lavas: inferences from geochemical inverse modeling. Contributions to Mineralogy and Petrology, 113(2): 226–235, doi: 10.1007/BF00283230

Feigenson M D, Carr M J, Maharaj S V, et al. 2004. Lead isotope composition of Central American volcanoes: Influence of the Galapagos plume. Geochemistry, Geophysics, Geosystems, 5(6): Q06001, doi: 10.1029/2003GC000621

Gazel E, Carr M J, Hoernle K, et al. 2009. Galapagos-OIB signature in Southern Central America: Mantle refertilization by arc-hot spot interaction. Geochemistry, Geophysics, Geosystems, 10(2): Q02S11, doi: 10.1029/2008GC002246

Gazel E, Hoernle K, Carr M J, et al. 2011. Plume-subduction interaction in Southern Central America: Mantle upwelling and slab melting. Lithos, 121(1–4): 117–134, doi: 10.1016/j.lithos.2010.10.008

Ge Zhenmin, Yan Quanshu, Zhao Renjie, et al. 2020. Mineral chemistry and geological significance of plagioclases hosted by basalts from the Cocos Ridge. Haiyang Xuebao (in Chinese), 42(7): 93–107

Goss A R, Kay S M, 2006. Steep REE patterns and enriched Pb isotopes in Southern Central American arc magmas: Evidence for forearc subduction erosion?. Geochemistry, Geophysics, Geosystems, 7(5): Q05016, doi: 10.1029/2005GC001163

Harpp K S, Wanless V D, Otto R H, et al. 2005. The Cocos and Carnegie aseismic ridges: a trace element record of long-term plume-spreading center interaction. Journal of Petrology, 46(1): 109–133, doi: 10.1093/petrology/egh064

Harris R N, Sakaguchi A, Petronotis K, et al. 2013. Costa Rica seismogenesis project, Program A Stage 2 (CRISP–A2). In: Proceedings of the Integrated Ocean Drilling Program, Expedition 344. College Station, TX, USA: Integrated Ocean Drilling Program, doi: 10.2204/iodp.proc.344.2013

Hoernle K, Abt D L, Fischer K M, et al. 2008. Arc-parallel flow in the mantle wedge beneath Costa Rica and Nicaragua. Nature, 451(7182): 1094–1097, doi: 10.1038/nature06550

Hoernle K, Werner R, Morgan J P, et al. 2000. Existence of complex spatial zonation in the Galápagos plume. Geology, 28(5): 435–438, doi: 10.1130/0091-7613(2000)28<435:EOCSZI>2.0.CO;2

Johnson M C, Plank T. 2000. Dehydration and melting experiments constrain the fate of subducted sediments. Geochemistry, Geophysics, Geosystems, 1(12): 1007, doi: 10.1029/1999GC000014

Li Yongxiang, Zhao Xixi, Jovane L G, et al. 2015. Paleomagnetic constraints on the tectonic evo-lution of the Costa Rican subduction zone: New results from sedimentary successions of IODP drill sites from the Cocos Ridge. Geochemistry, Geophysics, Geosystems, 16(12): 4479–4493, doi: 10.1002/2015GC006058

Li Yongxiang, Zhao Xixi, Xie Siyi, et al. 2018. Paleomagnetism of IODP Site U1380: implications for the forearc deformation in the Costa Rican erosive convergent margin. Scientific Reports, 8: 11430, doi: 10.1038/s41598-018-29243-7

Lyle M, Dadey K A, Farrell J W. 1995. The late Miocene (11–8 Ma) eastern Pacific carbonate crash: evidence for reorganization of deep-water circulation by the closure of the Panama gateway. In: Pisias N G, Mayer L A, Janecek T R, et al., eds. Proceeding of the Ocean Drilling Program, Scientific Results, Vol. 138. College Station, TX, USA: Ocean Drilling Program, 821–838

Maria I S, Demetrio B, Baxter A T, et al. 2017. Neogene paleoceanography of the eastern equatorial Pacific based on the radiolarian record of IODP drill sites off Costa Rica. Geochemistry, Geophysics, Geosystems, 18(3): 889–906, doi:10.1002/2016GC006623

Morell K D. 2016. Seamount, ridge, and transform subduction in Southern Central America. Tectonics, 35(2): 357–385, doi: 10.1002/2015TC003950

Newkirk D R, Martin E E. 2009. Circulation through the Central American Seaway during the Miocene carbonate crash. Geology, 37(1): 87–90, doi: 10.1130/G25193A.1

Nielsen S G, Prytulak J, Blusztajn J, et al. 2017. Thallium isotopes as tracers of recycled materials in subduction zones: Review and new data for lavas from Tonga-Kermadec and Central America. Journal of Volcanology and Geothermal Research, 339: 23–40, doi: 10.1016/j.jvolgeores.2017.04.024

Patino L C, Carr M J, Feigenson M D. 2000. Local and regional variations in Central American arc lavas controlled by variations in subducted sediment input. Contributions to Mineralogy and Petrology, 138(3): 265–283, doi: 10.1007/s004100050562

Pearce J A, Stern R J. 2006. Origin of back-arc basin magmas: trace element and isotope perspectives. In: Back-Arc Spreading Systems: Geological, Biological, Chemical, and Physical Interactions. Washington, D. C: American Geophysical Union, 166: 63–86, doi: 10.1029/166GM06

Pearce J A, Stern R J, Bloomer S H, et al. 2005. Geochemical mapping of the Mariana arc-basin system: Implications for the nature and distribution of subduction components. Geochemistry, Geophysics, Geosystems, 6(7): Q07006, doi: 10.1029/2004GC000895

Plank T. 2005. Constraints from thorium/lanthanum on sediment recycling at subduction zones and the evolution of the continents. Journal of Petrology, 46(5): 921–944, doi: 10.1093/petrology/egi005

Plank T. 2014. The chemical composition of subducting sediments. In: Holland H D, Turekian K K, eds. Treatise on Geochemistry. 2nd ed. Oxford, UK: Elsevier, 607–629, doi: 10.1016/B978-0-08-095975-7.00319-3

Plank T, Balzer V, Carr M. 2002. Nicaraguan volcanoes record paleoceanographic changes accompanying closure of the Panama Gateway. Geology, 30(12): 1087–1090, doi: 10.1130/0091-7613(2002)030<1087:NVRPCA>2.0.CO;2

Plank T, Kelley K A, Murray R W, et al. 2007. Chemical composition of sediments subducting at the Izu-Bonin trench. Geochemistry, Geophysics, Geosystems, 8(4): Q04I16, doi: 10.1029/2006GC001444

Plank T, Langmuir C H. 1998. The chemical composition of subduct-

ing sediment and its consequences for the crust and mantle. Chemical Geology, 145(4–5): 325–394, doi: 10.1016/S0009-2541(97)00150-2

Plank T, Manning C E. 2019. Subducting carbon. Nature, 574(7778): 343–352, doi: 10.1038/s41586-019-1643-z

Protti M, Guendel F, McNally K. 1995. Correlation between the age of the subducting Cocos plate and the geometry of the Wadati-Benioff zone under Nicaragua and Costa Rica, In: Mann P, ed. Geologic and Tectonic Development of the Carribbean Plate Boundary in Southern Central America. Boulder, CO, USA: Geological Society of America, 309–326

Reijmer J J, Betzler C, Kroon D, et al. 2002. Bahamian carbonate platform development in response to sea-level changes and the closure of the Isthmus of Panama. International Journal of Earth Sciences, 91(3): 482–489, doi: 10.1007/s00531-001-0235-x

Rudnick R L, Gao Shan. 2014. Composition of the continental crust. In: Holland H D, Turekian K K, eds. Treatise on Geochemistry. Oxford, UK: Elsevier, 1–51, doi: 10.1016/B978-0-08-095975-7.00301-6

Saginor I, Gazel E, Condie C, et al. 2013. Evolution of geochemical variations along the Central American volcanic front. Geochemistry, Geophysics, Geosystems, 14(10): 4504–4522, doi: 10.1002/ggge.20259

Sandoval M I, Boltovskoy D, Baxter A T, et al. 2017. Neogene paleoceanography of the eastern equatorial Pacific based on the radiolarian record of IODP drill sites off Costa Rica. Geochemistry, Geophysics, Geosystems, 18(3): 889–906, doi: 10.1002/2016GC006623

Schindlbeck J C, Kutterolf S, Freundt A, et al. 2015. The miocene galápagos ash layer record of Integrated Ocean Drilling Program legs 334 and 344: Ocean–island explosive volcanism during plume–ridge interaction. Geology, 43(7): 599–602, doi: 10.1130/G36645.1

Schindlbeck J C, Kutterolf S, Freundt A, et al. 2016a. Late Cenozoic tephrostratigraphy offshore the Southern Central American volcanic arc: 1. Tephra ages and provenance. Geochemistry, Geophysics, Geosystems, 17(11): 4641–4668, doi: 10.1002/2016GC006503

Schindlbeck J C, Kutterolf S, Freundt A, et al. 2016b. Late Cenozoic tephrostratigraphy offshore the Southern Central American volcanic arc: 2. Implications for magma production rates and subduction erosion. Geochemistry, Geophysics, Geosystems, 17(11): 4585–4604, doi: 10.1002/2016GC006504

Solomon E, Kastner M, Robertson G, 2006. Barium cycling at the convergent Costa Rican Margin. In: Morris J D, ed. Proceedings of Ocean Drilling Program, Scientific Results, Vol. 205. College Station, TX, USA: Ocean Drilling Program,

Spandler C, Pirard C. 2013. Element recycling from subducting slabs to arc crust: A review. Lithos, 170–171: 208–223, doi: 10.1016/j.lithos.2013.02.016

Stone R. 2013. Battle for the Americas. Science, 341(6143): 230–233, doi: 10.1126/science.341.6143.230

Straub S M, Gómez-Tuena A, Bindeman I N, et al. 2015. Crustal recycling by subduction erosion in the central Mexican Volcanic Belt. Geochimica et Cosmochimica Acta, 166: 29–52, doi: 10.1016/j.gca.2015.06.001

Sun S S, McDonough W F. 1989. Chemical and isotopic systematics of oceanic basalts: implications for mantle composition and processes. Geological Society, London, Special Publication, 42(1): 313–345, doi: 10.1144/gsl.sp.1989.042.01.19

Tera F, Brown L, Morris J, et al. 1986. Sediment incorporation in island-arc magmas: inferences from ^{10}Be. Geochimica et Cosmochimica Acta, 50(4): 535–550, doi: 10.1016/0016-7037(86)90103-1

Vannucchi P, Fisher D M, Bier S, et al. 2006. From seamount accretion to tectonic erosion: Formation of Osa mélange and the effects of Cocos Ridge subduction in southern Costa Rica. Tectonics, 25(2): TC2004, doi: 10.1029/2005TC001855

Vannucchi P, Morgan J P, Balestrieri M L. 2016. Subduction erosion, and the de-construction of continental crust: the Central America case and its global implications. Gondwana Research, 40: 184–198, doi: 10.1016/j.gr.2016.10.001

Vannucchi P, Sak P B, Morgan J P, et al. 2013. Rapid pulses of uplift, subsidence, and subduction erosion offshore Central America: Implications for building the rock record of convergent margins. Geology, 41(9): 995–998, doi: 10.1130/G34355.1

Vannucchi P, Ujiie K, Stroncik N, et al. 2012. Costa Rica Seismogenesis Project, Program A Stage 1 (CRISP–A1). In: Proceedings of the Integrated Ocean Drilling Program. College Station, TX, USA: Integrated Ocean Drilling Program, doi: 10.2204/iodp.proc.334.2012

Walker J A, Gazel E. 2014. Igneous rock associations 13. Focusing on the Central American subduction zone. Geoscience Canada, 41(1): 57–74, doi: 10.12789/geocanj.2014.41.036

Walther C H E. 2003. The crustal structure of the Cocos Ridge off Costa Rica. Journal of Geophysical Research: Solid Earth, 108(B3): 2136, doi: 10.1029/2001JB000888

Werner R, Hoernle K, Barckhausen U, et al. 2003. Geodynamic evolution of the Galápagos hot spot system (central East Pacific) over the past 20 m. y. : Constraints from morphology, geochemistry, and magnetic anomalies. Geochemistry, Geophysics, Geosystems, 4(12): 1108, doi: 10.1029/2003GC000576

Workman R K, Hart S R. 2005. Major and trace element composition of the depleted MORB mantle (DMM). Earth and Planetary Science Letters, 231(1–2): 53–72, doi: 10.1016/j.epsl.2004.12.005

Yan Quanshu, Shi Xuefa. 2014. Geological effects of aseismic ridges or seamount chains subduction on the supra-subduction zone. Haiyang Xuebao, 36(5): 107–123, doi: 10.3969/j.issn.0253-4193.2014.05.012

Yan Quanshu, Zhang Pingyang, Metcalfe I, et al. 2019. Geochemistry of axial lavas from the mid- and southern Mariana Trough, and implications for back-arc magmatic processes. Mineralogy and Petrology, 113(6): 803–820, doi: 10.1007/s00710-019-00683-x

Zhang Haitao, Yan Quanshu, Li Chuanshun, et al. 2019. Geochemistry of diverse lava types from the Lau Basin (South West Pacific): Implications for complex back-arc mantle dynamics. Geological Journal, 54(6): 3643–3659, doi: 10.1002/gj.3354

Zhao Renjie, Yan Quanshu, Zhang Haitao, et al. 2020. The chemical composition of global subducting sediments and its geological significance. Advances in Earth Science, 35(8): 789–803, doi: 10.11867/j.issn.1001-8166.2020.068

Zhao Renjie, Yan Quanshu, Zhang Haitao, et al. 2021. Chemical composition of sediments from the upper plate at the Southern Central American subduction zone and its geological significance. Acta Petrologica Sinica, 37(7): 1949–1963, doi: 10.18654/1000-0569/2021.07.01

Appendix:

Table A1. The contents of major components (%, wt%) and trace elements (10^{-6}) of Holes U1381C and U1414A

	Hole U1381C											Hole U1414A															
	Unit I core section						Unit II core section					Unit IA core section									Unit IB core section						
	1H-4	2H-4	3H-4	4H-4	5H-4	6H-4	7H-4	8H-4	9H-4	10H-4	11H-4	1H-2	2H-4	3H-4	4H-4	5H-4	6H-3	7H-2	8H-6	9H-4	10H-3	11H-3	12H-2	13H-2	14H-4	15H-4	16H-1
Depth/cm	83–85	94–96	98–100	54–56	82–84	66–68	60–62	66–68	86–88	68–70	74–76	69–71	83–84	39–40	44–46	138–140	142–144	88–100	117–119	38–40	69–71	52–54	88–90	69–71	54–55	67–68	106–107
Major element																											
SiO_2	48.34	45.56	49.20	48.48	48.84	37.60	45.26	36.42	32.94	38.30	32.36	27.42	11.36	38.64	8.70	48.00	46.82	49.14	48.12	–	47.90	46.12	43.84	49.11	52.04	46.00	48.12
TiO_2	0.96	0.89	0.96	0.97	0.90	0.56	0.24	0.47	0.31	0.29	0.33	0.12	0.25	0.21	0.14	0.93	0.95	0.77	0.94	0.95	0.98	0.92	0.89	0.95	0.91	0.92	0.91
Al_2O_3	15.36	14.41	15.67	11.67	14.93	11.05	2.38	4.50	2.74	0.64	2.88	1.47	2.62	2.07	1.17	14.55	14.23	13.85	15.24	15.28	15.34	14.73	14.56	15.36	17.05	14.58	14.22
TFe_2O_3	8.38	7.80	8.67	8.80	8.10	5.05	2.11	4.12	2.57	3.16	3.47	1.04	2.43	2.14	1.93	8.50	9.04	8.09	8.99	7.87	8.88	8.99	8.20	8.49	7.65	9.67	8.61
MnO	0.06	0.06	0.05	0.06	0.06	0.05	0.06	0.10	0.10	0.12	0.16	0.03	0.27	0.20	0.43	0.09	0.07	0.06	0.09	0.06	0.07	0.07	0.09	0.06	0.15	0.07	0.07
MgO	3.79	3.41	3.63	2.78	3.57	2.62	0.96	1.77	1.09	1.20	2.70	2.33	14.81	10.44	2.52	4.14	3.75	3.06	3.78	3.59	3.86	3.55	3.35	3.60	3.39	3.55	3.55
CaO	3.40	6.69	3.25	3.83	5.38	18.05	20.80	23.09	26.95	20.89	25.29	32.71	22.44	15.23	41.22	4.29	5.03	4.07	4.67	4.62	3.61	5.83	7.88	3.19	2.86	5.66	5.03
Na_2O	3.45	3.03	3.37	3.22	3.12	2.60	2.87	2.58	2.14	2.49	2.16	0.79	0.52	0.62	0.29	3.91	3.32	3.40	3.33	3.14	3.31	3.17	2.87	3.22	3.33	3.12	3.11
K_2O	1.69	1.57	1.74	1.37	1.66	1.26	0.32	0.57	0.39	0.41	0.32	0.36	0.42	0.42	0.23	1.54	1.55	1.58	1.60	1.67	1.68	1.58	1.44	1.49	1.76	1.40	1.55
P_2O_5	0.18	0.17	0.17	0.14	0.15	0.14	0.16	0.15	0.12	0.16	0.18	0.10	0.10	0.13	0.08	0.20	0.16	0.15	0.21	0.16	0.19	0.16	0.17	0.14	0.14	0.15	0.15
LOI	13.02	14.52	12.32	11.97	–	18.60	21.70	–	24.37	25.33	23.60	30.50	38.12	27.61	–	14.03	12.92	12.60	12.29	–	13.95	13.52	14.74	11.81	10.74	13.36	12.15
Trace element																											
Li	85.42	79.68	83.31	82.00	76.65	44.89	5.42	9.09	7.40	9.59	8.10	12.57	19.01	5.43	5.88	69.04	68.87	65.41	72.21	78.31	74.01	73.66	66.18	77.61	78.57	70.07	65.87
Be	0.93	0.97	0.87	0.83	0.83	0.76	0.27	0.48	0.37	0.40	0.32	0.37	0.47	0.47	0.19	0.75	0.82	0.79	0.78	0.81	0.78	0.73	0.70	0.73	0.80	0.70	0.74
Cr	108.76	98.40	108.40	108.76	101.31	60.60	23.82	33.37	30.44	36.79	28.72	15.20	21.92	35.52	14.69	122.14	124.07	90.04	103.44	98.41	111.34	93.63	125.90	103.33	77.41	106.03	103.81
Co	21.20	20.08	24.10	24.43	23.46	21.82	8.48	15.07	8.94	8.67	10.72	4.25	7.81	5.80	5.90	24.96	21.28	18.39	27.29	19.90	22.77	22.27	23.31	22.98	27.42	25.09	23.23
Ni	61.00	56.83	64.10	67.84	65.01	54.59	34.10	41.31	41.30	46.54	39.82	31.63	41.95	43.65	38.30	74.36	61.46	64.36	93.20	52.63	63.54	66.90	74.61	63.60	66.40	78.32	69.16
Cu	70.19	67.70	74.57	78.81	68.83	51.30	23.10	48.47	33.64	40.95	38.98	21.15	28.81	33.45	22.66	75.28	58.69	61.96	80.58	71.84	70.33	66.42	70.62	79.92	86.69	77.53	68.15
Zn	140.74	126.81	150.13	152.05	210.70	94.42	66.62	92.94	94.25	94.96	120.45	85.54	87.43	83.59	68.34	150.41	158.05	111.25	161.07	129.75	139.97	136.64	134.70	137.28	132.98	138.15	138.90
Ga	17.55	16.77	18.17	18.16	17.37	13.03	3.51	6.63	4.31	4.30	4.06	2.68	5.49	3.80	2.20	17.29	17.09	16.96	17.81	17.84	18.35	17.45	17.15	19.18	20.65	17.39	17.40
Ge	1.38	1.25	1.40	1.36	1.30	0.97	0.63	0.72	0.64	0.75	0.82	0.36	1.07	0.42	0.22	1.23	1.16	1.17	1.23	1.16	1.22	1.22	1.31	1.36	1.37	1.25	1.30
Ba	758.68	633.28	808.37	743.52	840.94	894.19	740.24	689.34	749.70	929.00	895.97	1 241.07	90.03	61.77	45.89	850.58	536.01	642.72	1 063.09	703.43	817.02	788.72	574.35	872.48	408.18	923.73	989.60
Sr	222.09	301.55	229.11	217.79	307.54	689.02	682.66	789.72	927.30	739.47	832.40	1 067.47	221.11	235.66	146.36	256.62	247.45	274.77	273.92	250.48	233.20	292.43	339.17	193.30	248.62	251.94	251.06
Nb	7.51	7.15	7.46	6.97	7.72	5.84	3.45	7.14	5.61	4.49	3.21	2.49	4.34	2.59	1.38	6.89	6.89	6.30	7.23	7.08	7.53	6.73	6.57	6.66	6.66	6.54	7.14
Mo	3.72	2.20	2.51	1.42	1.66	1.68	3.94	10.65	11.29	10.60	7.37	5.08	8.18	10.94	4.33	0.95	1.98	2.22	1.05	1.61	1.49	1.86	1.73	1.34	0.84	1.67	1.36
Cd	0.39	0.33	0.47	0.35	0.30	0.35	0.42	0.52	0.78	0.49	0.37	0.38	0.46	0.71	0.30	0.34	0.28	0.33	0.35	0.41	0.27	0.28	0.40	0.30	0.19	0.27	0.25
In	0.06	0.05	0.06	0.06	0.06	0.04	0.02	0.04	0.03	0.03	0.04	0.02	0.02	0.02	0.01	0.06	0.06	0.05	0.06	0.06	0.06	0.06	0.06	0.08	0.06	0.06	0.06
Cs	1.79	1.77	1.89	1.19	1.88	1.30	0.11	0.23	0.17	0.19	0.16	0.23	0.30	0.47	0.13	1.48	1.57	1.50	1.60	1.73	1.69	1.69	1.60	1.73	1.67	1.63	1.77
Hf	3.03	3.00	3.08	3.04	2.90	2.14	0.94	1.60	1.21	1.29	0.79	0.43	0.97	0.61	0.27	2.36	2.37	2.36	2.38	2.47	2.52	2.34	2.16	2.37	2.41	2.12	2.23
Zr	102.32	99.91	109.31	103.08	101.38	73.51	34.97	54.31	45.36	48.55	26.92	15.78	34.75	22.27	7.96	84.95	81.79	79.41	89.61	90.73	92.47	89.80	85.52	85.50	88.10	81.47	85.78
Ta	0.48	0.47	0.51	0.49	0.49	0.45	0.27	0.48	0.39	0.28	0.21	0.20	0.33	0.19	0.11	0.43	0.42	0.38	0.42	0.41	0.44	0.38	0.39	0.38	0.41	0.39	0.43

to be continued

Continued form Table A1

	Hole U1381C											Hole U1414A															
	Unit I core section						Unit II core section					Unit IA core section									Unit IB core section						
	1H-4	2H-4	3H-4	4H-4	5H-4	6H-4	7H-4	8H-4	9H-4	10H-4	11H-4	1H-2	2H-4	3H-4	4H-4	5H-4	6H-3	7H-2	8H-6	9H-4	10H-3	11H-3	12H-2	13H-2	14H-4	15H-4	16H-1
W	0.38	0.37	0.38	0.36	0.46	0.29	0.07	0.12	0.11	0.09	0.08	0.11	0.36	0.24	0.12	0.40	0.34	0.33	0.42	0.38	0.43	0.36	0.41	0.36	0.38	0.34	0.36
Tl	0.19	0.17	0.25	0.17	0.23	0.26	0.07	0.11	0.18	0.10	0.09	0.15	0.25	0.41	0.13	0.25	0.17	0.20	0.35	0.16	0.16	0.17	0.18	0.14	0.15	0.13	0.15
Pb	5.75	5.90	6.55	6.30	8.52	5.59	1.69	3.33	2.44	3.50	2.41	3.86	3.55	3.13	1.47	5.52	5.19	5.20	6.12	5.30	5.42	5.52	4.77	5.02	6.11	4.72	5.05
Bi	0.07	0.07	0.08	0.08	0.08	0.06	0.03	0.04	0.03	0.04	0.04	0.04	0.04	0.05	0.02	0.07	0.06	0.07	0.08	0.07	0.07	0.07	0.07	0.07	0.07	0.07	0.08
Th	2.58	2.56	2.73	0.81	2.97	2.65	0.40	0.77	0.62	0.38	0.34	0.52	0.59	0.43	0.17	2.24	2.03	2.30	2.44	2.41	2.63	2.35	2.35	2.13	3.12	1.89	2.19
U	5.38	6.04	4.94	4.22	5.06	7.84	5.33	7.19	7.17	4.12	3.69	3.55	5.01	5.15	3.96	3.21	3.75	4.46	5.43	4.82	3.90	3.57	3.79	3.04	1.79	3.23	3.15
Sc	28.76	26.93	28.64	11.10	27.62	17.39	7.55	13.28	8.19	1.81	10.44	3.46	8.75	6.62	6.10	27.34	27.57	23.24	26.47	26.75	28.58	27.66	26.64	30.42	26.49	27.97	26.62
V	174.95	163.91	176.97	190.69	169.70	114.95	65.89	119.18	81.26	86.65	94.06	28.36	106.92	94.70	60.68	175.39	170.77	144.22	175.42	175.02	182.85	168.59	163.78	183.04	161.98	172.18	163.49
La	13.14	13.50	13.98	9.17	13.82	13.40	4.41	8.08	6.51	5.33	5.11	10.36	6.63	6.93	5.94	12.45	11.55	12.57	13.69	12.90	14.30	12.90	12.39	11.38	13.18	10.84	11.89
Ce	27.01	27.22	27.82	21.88	28.55	26.41	7.23	13.80	9.58	8.70	6.64	15.82	9.81	8.15	5.55	24.97	22.29	23.91	27.46	25.99	27.62	24.74	24.45	24.14	29.11	22.99	24.77
Pr	3.53	3.56	3.61	2.76	3.57	3.23	1.11	2.12	1.50	1.22	1.15	2.38	1.63	1.35	1.02	3.33	3.19	3.21	3.57	3.48	3.69	3.35	3.28	3.13	3.55	2.97	3.13
Nd	14.84	14.99	15.11	12.08	14.70	13.04	4.86	9.30	6.35	5.28	5.20	9.29	7.26	5.99	4.34	14.11	13.67	13.22	14.77	14.50	15.45	14.03	13.66	13.11	14.47	12.53	12.98
Sm	3.46	3.43	3.50	2.90	3.26	2.73	1.27	2.34	1.53	1.30	1.36	1.84	1.66	1.35	0.96	3.23	3.15	2.95	3.32	3.29	3.45	3.08	3.06	3.11	3.34	2.89	2.98
Eu	1.16	1.11	1.19	1.02	1.12	1.01	0.53	0.79	0.60	0.58	0.61	0.62	0.50	0.39	0.30	1.15	1.06	1.02	1.19	1.11	1.17	1.08	0.99	1.08	1.05	1.03	1.04
Gd	3.23	3.25	3.38	2.84	3.09	2.58	1.36	2.46	1.65	1.43	1.49	1.85	1.69	1.48	1.07	3.10	2.98	2.72	3.15	3.06	3.16	2.95	2.90	2.89	2.99	2.77	2.77
Tb	0.58	0.59	0.61	0.51	0.55	0.42	0.26	0.48	0.30	0.28	0.29	0.30	0.31	0.29	0.21	0.55	0.54	0.48	0.56	0.52	0.56	0.51	0.49	0.51	0.52	0.48	0.47
Dy	3.69	3.76	3.85	3.32	3.44	2.59	1.79	3.27	2.06	2.04	2.01	1.90	2.06	2.03	1.45	3.44	3.32	2.97	3.42	3.31	3.50	3.17	3.06	3.17	3.14	3.02	2.90
Ho	0.72	0.73	0.75	0.66	0.66	0.49	0.37	0.67	0.42	0.43	0.42	0.39	0.42	0.43	0.32	0.66	0.63	0.57	0.66	0.63	0.67	0.61	0.58	0.58	0.58	0.58	0.55
Er	2.12	2.10	2.26	1.89	1.92	1.43	1.09	1.94	1.26	1.33	1.26	1.21	1.29	1.33	0.99	1.89	1.84	1.65	1.91	1.79	1.92	1.77	1.68	1.71	1.69	1.69	1.60
Tm	0.33	0.34	0.35	0.30	0.30	0.22	0.17	0.31	0.20	0.21	0.20	0.19	0.21	0.21	0.16	0.30	0.29	0.26	0.31	0.29	0.30	0.28	0.26	0.27	0.27	0.27	0.25
Yb	2.16	2.24	2.33	1.96	1.99	1.49	1.09	1.99	1.28	1.33	1.25	1.32	1.35	1.33	1.07	1.93	1.84	1.69	2.01	1.83	1.96	1.82	1.70	1.80	1.70	1.70	1.62
Lu	0.35	0.36	0.37	0.32	0.32	0.24	0.18	0.32	0.21	0.22	0.21	0.22	0.23	0.22	0.18	0.31	0.30	0.27	0.33	0.30	0.32	0.29	0.28	0.28	0.27	0.28	0.26
Y	20.39	21.11	21.65	14.47	18.41	14.54	11.70	21.36	14.19	11.88	14.64	14.16	14.17	16.02	12.21	18.36	17.37	16.07	19.10	17.69	19.55	18.25	17.09	16.98	15.75	17.06	15.72

	Hole U1414A																								BHVO-2 (measured)	BHVO-2 (recommended)
	Unit IIA core section						Unit IIB core section													Unit III core section							
	17H-6	18H-4	19H-2	20H-6	21H-6	22H-3	23X-4	24X-4	25X-4	26X-3	27X-6	28X-5	29X-6	30X-5	31X-6	32X-3	33X-1	34X-1	35X-1	36R-1	37R-5	39R-2	41R-2	42R-1	44R-1		
Depth/cm	133–134	94–96	39–41	34–36	121–123	75–77	72–74	65–67	65–67	99–101	63–64	144–145	141–142	117–119	73–75	89–91	7–10	68–71	102–106	87–91	81–82	41–43	106–107	25–26	69–71		
Major element																											
SiO_2	49.20	–	–	–	–	28.18	26.80	16.50	11.08	7.94	14.80	34.80	33.00	–	22.44	13.78	15.46	5.18	7.28	11.18	12.08	10.78	9.36	24.24	16.98	49.87	49.9
TiO_2	0.91	0.80	0.68	0.61	0.58	0.45	0.40	0.24	0.14	0.10	0.20	0.50	0.56	0.52	0.20	0.11	0.10	0.04	0.04	0.04	0.02	0.15	0.19	0.13	0.09	2.71	2.73
Al_2O_3	15.10	13.16	12.27	10.80	10.18	7.88	6.87	4.48	2.85	1.92	2.38	5.12	5.40	5.62	2.55	1.80	1.24	0.54	0.51	0.59	0.33	1.55	1.76	1.32	0.81	13.60	13.50
TFe_2O_3	8.23	7.63	5.86	5.19	5.00	4.26	3.68	2.25	1.36	1.04	1.35	3.88	3.80	3.92	2.03	1.30	0.89	0.47	0.29	0.56	0.37	1.57	1.61	0.86	0.72	12.28	12.30
MnO	0.07	0.05	0.05	0.05	0.05	0.04	0.04	0.03	0.03	0.03	0.04	0.05	0.06	0.03	0.03	0.03	0.03	0.03	0.04	0.04	0.05	0.03	0.04	0.05	0.04	–	–
MgO	3.80	3.25	2.83	2.51	2.54	1.95	1.73	1.14	0.77	0.81	0.84	1.88	2.07	1.86	1.21	0.62	0.54	0.36	0.26	0.43	0.30	0.84	0.82	0.37	0.45	7.25	7.23
CaO	4.89	10.57	12.22	17.29	18.45	25.28	26.20	37.66	41.58	45.08	40.32	24.40	25.72	21.58	33.99	41.43	40.93	44.01	47.60	44.36	45.34	43.32	43.96	36.15	40.78	11.5	11.40

to be continued

Continued form Table A1

	Hole U1414A																									
	Unit IIA core section						Unit IIB core section													Unit III core section						BHVO-2 (measured)	BHVO-2 (recommended)
	17H-6	18H-4	19H-2	20H-6	21H-6	22H-3	23X-4	24X-4	25X-4	26X-3	27X-6	28X-5	29X-6	30X-5	31X-6	32X-3	33X-1	34X-1	35X-1	36R-1	37R-5	39R-2	41R-2	42R-1	44R-1		
Depth/cm	133–134	94–96	39–41	34–36	121–123	75–77	72–74	65–67	65–67	99–101	63–64	144–145	141–142	117–119	73–75	89–91	7–10	68–71	102–106	87–91	81–82	41–43	106–107	25–26	69–71		
Na_2O	3.33	2.75	2.48	2.32	2.27	1.87	1.61	1.16	0.83	0.89	1.35	2.23	2.27	1.86	1.62	1.12	1.06	0.69	0.64	0.83	0.67	0.76	0.77	0.80	0.60	2.22	2.22
K_2O	1.64	1.43	1.38	1.23	1.17	0.80	0.94	0.61	0.46	0.26	0.36	0.68	0.58	0.74	0.47	0.34	0.20	0.09	0.14	0.17	0.09	0.36	0.45	0.43	0.24	0.53	0.52
P_2O_5	0.16	0.13	0.14	0.17	0.16	0.16	0.15	0.20	0.15	0.13	0.43	0.28	0.20	0.33	0.24	0.15	0.15	0.12	0.12	0.15	0.10	0.12	0.12	0.12	0.08	0.26	0.27
LOI	11.12	–	–	–	–	25.36	27.00	33.79	37.21	39.49	35.29	23.67	24.30	–	31.86	36.01	35.92	40.76	40.39	37.14	39.51	–	37.22	31.37	35.13	–	–
Trace element																											
Li	80.59	66.94	68.11	51.08	51.99	40.38	30.89	19.07	11.18	12.53	11.10	24.35	20.51	25.85	15.57	8.91	9.00	7.11	4.75	11.01	4.53	12.43	11.91	7.07	5.95	–	–
Be	0.76	0.80	0.74	0.55	0.77	0.57	0.60	0.41	0.34	0.24	0.40	0.74	0.63	0.78	0.46	0.31	0.25	0.11	0.16	0.17	0.13	0.29	0.38	0.53	0.17	–	–
Cr	103.81	87.80	67.32	69.98	69.52	53.47	47.50	25.80	18.58	12.74	16.23	42.38	55.15	54.40	24.67	10.48	11.19	6.27	6.56	6.38	3.96	17.19	13.92	11.96	11.96	278.00	280.00
Co	26.31	24.73	20.43	21.27	18.45	19.73	17.46	11.87	6.99	6.69	10.29	21.41	21.56	19.92	11.86	6.51	6.64	3.48	5.45	4.25	3.15	6.53	6.59	4.71	4.38	44.80	45.00
Ni	78.20	62.88	56.62	55.36	59.29	68.66	60.28	41.54	25.40	28.89	43.39	114.82	56.73	83.05	64.32	35.51	38.13	22.49	34.72	29.33	20.78	35.68	33.65	22.43	23.84	114.00	119.00
Cu	77.20	67.88	64.84	80.36	71.18	59.65	53.61	42.56	25.37	23.64	40.73	38.75	57.69	62.33	33.23	22.45	23.27	12.56	15.69	16.53	11.87	23.47	22.09	14.98	15.99	126.00	127.00
Zn	154.07	120.50	138.47	120.82	147.20	89.77	74.15	57.40	34.74	43.50	103.48	89.11	123.37	151.54	80.62	53.80	55.46	28.95	39.87	33.82	17.89	53.49	87.32	48.78	35.44	104.00	103.00
Ga	18.39	16.11	15.33	13.05	12.41	9.52	8.79	5.59	3.60	2.49	3.68	7.80	8.37	8.95	4.52	2.72	2.23	1.04	1.11	1.63	0.75	2.66	3.19	2.47	1.43	–	–
Ge	1.18	1.10	1.19	0.93	1.08	0.73	0.82	0.60	0.37	0.30	0.58	1.09	1.18	1.45	0.73	0.31	0.34	0.16	0.11	0.16	0.10	0.30	0.40	0.34	0.28	–	–
Ba	337.61	2 554.81	173.35	201.84	5 372.62	2 369.53	2 802.69	1 806.29	1 791.19	1 633.03	2 991.86	3 624.48	76.14	4 760.59	3 521.54	1 575.94	2 212.31	1 244.66	1 959.64	2 373.27	1 928.75	1 501.08	1 460.84	1 309.23	1 111.77	127.00	130.00
Sr	289.02	402.11	426.11	587.11	717.47	830.25	896.89	1 154.92	1 138.07	1 310.28	1 280.04	802.69	912.80	993.94	1 241.02	1 197.97	1 265.36	1 246.64	1 331.81	1 180.83	993.01	1 280.04	1 278.46	1 083.79	1 081.92	388.00	389.00
Nb	7.39	7.00	6.13	4.93	4.76	3.99	3.62	2.27	2.00	1.05	2.86	6.18	6.43	7.95	4.32	2.05	1.68	0.75	0.72	0.87	0.56	4.96	10.27	5.73	1.80	17.80	18.00
Mo	1.33	0.74	0.83	1.18	0.87	1.11	0.59	0.45	0.56	0.31	0.47	0.67	0.66	1.34	1.66	3.58	1.63	1.44	1.45	1.07	0.81	3.76	1.98	1.04	1.43	–	–
Cd	0.36	0.62	0.49	0.31	0.87	0.61	0.51	0.33	0.16	0.19	0.62	0.22	0.56	0.68	0.32	0.30	0.49	0.27	0.28	0.19	0.17	0.34	0.59	0.21	0.24	–	–
In	0.06	0.06	0.05	0.05	0.06	0.04	0.04	0.02	0.01	0.02	0.02	0.04	0.04	0.04	0.02	0.01	0.01	0.00	0.01	0.00	0.00	0.01	0.02	0.01	0.01	–	–
Cs	1.58	1.85	1.80	1.41	1.71	1.28	1.37	0.86	0.49	0.33	0.36	0.73	0.64	0.88	0.65	0.36	0.20	0.08	0.08	0.14	0.08	0.14	0.18	0.32	0.13	–	–
Hf	2.36	2.05	1.96	1.56	2.00	1.59	1.41	0.85	0.62	0.39	0.67	1.36	1.40	1.71	0.92	0.53	0.39	0.17	0.21	0.22	0.13	0.80	1.21	0.77	0.35	4.08	4.10
Zr	80.16	80.73	74.63	64.40	73.28	55.49	46.36	32.43	27.91	15.26	29.41	55.63	55.94	80.78	38.13	19.80	16.08	8.17	9.06	11.02	5.71	31.67	50.78	28.47	14.99	175.00	172.00
Ta	0.42	0.44	0.37	0.29	0.46	0.36	0.38	0.29	0.25	0.22	0.27	0.46	0.45	0.54	0.33	0.24	0.19	0.13	0.16	0.13	0.11	0.41	0.72	0.32	0.17	1.42	1.40
W	0.40	0.37	0.40	0.33	0.42	0.30	0.34	0.23	0.24	0.12	0.20	0.29	0.45	0.37	0.29	0.18	0.10	0.07	0.16	0.13	0.12	0.12	0.17	0.19	0.15	–	–
Tl	0.22	0.31	0.30	0.22	0.25	0.41	0.30	0.15	0.10	0.05	0.14	0.19	0.18	0.22	0.13	0.18	0.11	0.06	0.05	0.06	0.05	0.14	0.10	0.07	0.06	–	–
Pb	6.04	5.33	6.14	4.82	6.80	5.16	5.53	4.05	3.50	2.07	4.14	6.12	4.79	7.63	5.87	3.46	2.30	2.51	1.77	2.68	1.67	3.13	2.75	2.75	1.76	–	–
Bi	0.08	0.08	0.09	0.07	0.11	0.07	0.08	0.07	0.06	0.04	0.08	0.12	0.09	0.13	0.12	0.06	0.04	0.04	0.03	0.04	0.03	0.03	0.04	0.04	0.02	–	–
Th	2.80	2.09	2.37	1.52	1.75	1.51	1.23	0.87	0.73	0.43	0.66	1.08	0.92	1.32	1.02	0.71	0.30	0.14	0.15	0.21	0.15	0.61	0.94	0.57	0.20	1.15	1.20
U	3.84	7.35	5.55	4.50	4.50	6.76	3.23	2.85	2.51	2.00	4.52	5.29	4.61	5.35	3.22	2.20	2.16	1.44	1.53	1.46	1.15	3.12	2.73	1.88	2.05	–	–
Sc	26.95	24.87	21.89	19.61	20.12	15.99	15.04	9.32	6.16	4.38	7.18	14.64	16.80	16.36	8.37	5.30	5.08	2.43	2.61	2.86	2.15	4.05	4.21	3.58	3.24	31.60	32.00
V	167.55	180.48	136.95	124.48	147.06	103.53	101.33	60.80	29.80	27.08	50.05	105.10	114.39	107.95	66.50	28.80	29.80	13.20	18.36	20.30	12.11	34.15	31.61	25.79	23.38	312.00	317.00
La	13.99	12.30	12.71	11.88	11.86	12.39	10.21	8.24	8.37	4.88	11.93	13.63	11.23	16.32	12.80	8.18	6.36	4.11	4.35	5.96	3.77	7.82	10.82	11.99	4.59	14.76	15.00

to be continued

Continued form Table A1

	Hole U1414A																									
	Unit IIA core section						Unit IIB core section												Unit III core section						BHVO-2 (measured)	BHVO-2 (recommended)
	17H-6	18H-4	19H-2	20H-6	21H-6	22H-3	23X-4	24X-4	25X-4	26X-3	27X-6	28X-5	29X-6	30X-5	31X-6	32X-3	33X-1	34X-1	35X-1	36R-1	37R-5	39R-2	41R-2	42R-1	44R-1		
Depth/cm	133–134	94–96	39–41	34–36	121–123	75–77	72–74	65–67	65–67	99–101	63–64	144–145	141–142	117–119	73–75	89–91	7–10	68–71	102–106	87–91	81–82	41–43	106–107	25–26	69–71		
Ce	28.50	23.91	24.74	20.25	19.84	17.85	15.40	9.97	9.81	4.98	10.37	15.63	13.39	18.08	11.35	6.32	4.48	2.30	2.29	2.86	1.98	8.20	14.62	17.78	3.96	37.80	38.00
Pr	3.55	3.09	3.11	2.81	2.75	2.67	2.30	1.63	1.49	0.88	1.97	2.78	2.31	3.24	2.34	1.46	1.11	0.69	0.80	0.99	0.58	1.53	2.24	2.46	0.82	–	–
Nd	14.41	12.82	12.74	11.97	11.81	11.18	9.76	6.81	5.94	3.72	8.51	11.97	10.26	14.12	10.30	6.35	4.85	3.07	3.06	4.39	2.51	6.49	8.98	9.95	3.55	24.80	25.00
Sm	3.13	2.83	2.69	2.64	2.75	2.58	2.19	1.51	1.27	0.82	1.84	2.73	2.35	3.13	2.24	1.37	1.09	0.68	0.80	0.96	0.54	1.38	1.85	2.12	0.79	5.98	6.20
Eu	0.99	1.29	0.81	0.78	2.13	1.32	1.32	0.92	0.80	0.66	1.31	1.78	0.74	2.06	1.53	0.73	0.88	0.54	0.74	0.91	0.68	0.77	0.85	0.80	0.50	–	–
Gd	2.88	2.87	2.55	2.53	3.41	2.82	2.57	1.77	1.46	1.06	2.41	3.46	2.48	4.20	2.88	1.63	1.46	0.81	0.95	1.23	0.75	1.63	2.01	2.31	0.95	6.28	6.30
Tb	0.50	0.45	0.44	0.43	0.48	0.47	0.40	0.28	0.22	0.16	0.39	0.55	0.49	0.67	0.48	0.27	0.23	0.14	0.15	0.21	0.12	0.27	0.33	0.37	0.17	0.89	0.80
Dy	3.07	2.75	2.77	2.78	3.29	3.09	2.67	1.89	1.52	1.14	2.88	3.87	3.35	4.68	3.48	1.96	1.68	1.03	1.07	1.53	0.92	1.79	2.18	2.34	1.15	–	–
Ho	0.59	0.52	0.52	0.55	0.67	0.68	0.57	0.43	0.35	0.29	0.71	0.80	0.75	1.07	0.78	0.45	0.38	0.24	0.25	0.35	0.22	0.38	0.45	0.47	0.25	1.05	1.04
Er	1.80	1.55	1.56	1.62	2.02	2.09	1.73	1.39	1.13	0.94	2.33	2.85	2.34	3.33	2.47	1.37	1.23	0.74	0.80	1.10	0.71	1.16	1.42	1.38	0.77	–	–
Tm	0.27	0.25	0.25	0.25	0.33	0.33	0.28	0.23	0.19	0.16	0.37	0.45	0.38	0.53	0.40	0.22	0.20	0.12	0.13	0.17	0.12	0.18	0.22	0.21	0.12	–	–
Yb	1.72	1.57	1.59	1.65	2.12	2.17	1.81	1.49	1.21	0.98	2.33	2.87	2.44	3.45	2.59	1.42	1.27	0.77	0.84	1.12	0.75	1.17	1.38	1.33	0.79	1.95	2.00
Lu	0.28	0.26	0.26	0.27	0.36	0.37	0.31	0.26	0.21	0.17	0.41	0.52	0.43	0.60	0.44	0.25	0.22	0.13	0.15	0.19	0.13	0.19	0.23	0.22	0.13	0.28	0.28
Y	17.02	16.51	17.18	20.39	23.59	25.47	21.02	19.60	16.67	14.92	36.45	38.57	30.25	44.81	34.06	20.13	17.84	11.52	12.41	16.46	10.91	16.66	18.11	18.22	10.80	25.80	26.00

Note: TFe_2O_3 represents total content of Fe_2O_3; –, no data; LOI, loss on ignition.

Table A2. The lithological parameters of each unit of Holes U1381C and U1414A

Hole	U1381C			U1414A					
	Unit I	Unit II	Bulk	Unit IA	Unit IB	Unit IIA	Unit IIB	Unit III	Bulk
Thickness/m	55.93	44.71	100.64	78.30	67.04	54.67	109.36	65.88	375.25
Wet bulk density/(g·cm^{-3})	1.44	1.35	1.39	1.45	1.51	1.68	1.62	1.93	1.63
Water/%	0.75	0.78	0.77	0.74	0.71	0.61	0.63	0.44	0.63
Dry bulk density/(g·cm^{-3})	0.36	0.30	0.33	0.38	0.44	0.66	0.60	1.09	0.62
Sample amount	6	5	11	9	7	6	13	6	41
Mass proportion/%	60	40	100	13	13	16	28	30	100

Table A3. The major components (%, wt%) and trace elements (10^{-6}) of Holes U1381C and U1414A

	Hole U1381C						Hole U1414A											
	Unit I	RSD	Unit II	RSD	Bulk	RSD	Unit IA	RSD	Unit IB	RSD	Unit IIA	RSD	Unit IIB	RSD	Unit III	RSD	Bulk	RSD
Major element																		
SiO_2	46.34	±10%	37.06	±43%	42.65	±16%	34.77	±0.56%	47.59	±0.06%	38.69	±0.54%	17.44	±0.61%	14.10	±0.4%	26.01	±70%
TiO_2	0.87	±18%	0.33	±30%	0.66	±47%	0.59	±66%	0.92	±3%	0.67	±24%	0.24	±78%	0.10	±62%	0.40	±89%
Al_2O_3	13.85	±14%	2.63	±61%	9.39	±65%	8.94	±76%	15.12	±6%	11.58	±22%	3.17	±66%	1.06	±54%	6.19	±98%
TFe_2O_3	7.80	±18%	3.09	±45%	5.93	±46%	5.56	±63%	8.64	±7%	6.03	±26%	2.02	±67%	0.95	±55%	3.66	±90%
MnO	0.06	±8%	0.11	±30%	0.08	±43%	0.14	±93%	0.08	±41%	0.05	±23%	0.04	±22%	0.04	±13%	0.06	±123%
MgO	3.30	±15%	1.55	±55%	2.60	±41%	5.38	±80%	3.55	±5%	2.79	±22%	1.08	±57%	0.53	±44%	2.07	±129%
CaO	6.77	±84%	23.41	±41%	13.38	±73%	14.92	±95%	4.87	±37%	14.78	±48%	36.19	±24%	42.32	±8%	27.77	±59%
Na_2O	3.13	±10%	2.45	±41%	2.86	±16%	2.15	±71%	3.16	±5%	2.50	±20%	1.33	±41%	0.72	±11%	1.68	±67%
K_2O	1.55	±12%	0.40	±36%	1.09	±56%	1.04	±63%	1.56	±8%	1.29	±19%	0.45	±56%	0.29	±51%	0.76	±77%
P_2O_5	0.16	±11%	0.15	±16%	0.16	±12%	0.14	±32%	0.16	±12%	0.15	±9%	0.20	±46%	0.12	±19%	0.16	±42%
LOI	14.09	±44%	23.75	±51%	17.93	±50%	21.15	±62%	12.90	±11%	25.36	±57%	33.81	±32%	36.07	±42%	28.77	±50%
CO_2	4.39	±88%	17.94	±12%	9.77	±76%	2.34	±58%	5.86	±79%	24.89	±27%	29.67	±30%	30.31	±20%	22.45	–
H_2O	9.70	–	5.81	–	8.15	–	18.82	–	7.03	–	0.47	–	4.13	–	5.77	–	6.32	–
Trace element																		
Li	75.33	±20%	7.92	±44%	48.54	±76%	44.08	±73%	72.28	±7%	58.18	±21%	15.45	±52%	8.82	±38%	31.41	±91%
Be	0.87	±9%	0.37	±36%	0.67	±40%	0.60	±39%	0.74	±5%	0.68	±14%	0.42	±52%	0.28	±56%	0.48	±48%
Cr	97.71	±19%	30.62	±43%	71.05	±53%	69.49	±67%	103.07	±15%	75.30	±24%	25.54	±71%	10.90	±45%	44.90	±92%
Co	22.51	±8%	10.38	±47%	17.69	±38%	15.07	±60%	23.87	±8%	21.82	±14%	11.55	±56%	4.94	±28%	13.27	±63%
Ni	61.56	±8%	40.61	±42%	53.24	±22%	55.73	±35%	68.93	±8%	63.50	±14%	49.94	±52%	27.62	±22%	48.64	±44%
Cu	68.57	±14%	37.03	±47%	56.03	±33%	50.49	±47%	74.24	±10%	68.52	±9%	34.76	±46%	17.49	±25%	42.16	±58%
Zn	145.81	±26%	93.84	±45%	125.16	±32%	115.05	±31%	136.95	±2%	128.47	±18%	72.01	±51%	46.12	±51%	87.31	±50%
Ga	16.84	±12%	4.56	±46%	11.96	±55%	11.24	±65%	18.23	±7%	14.13	±22%	4.68	±62%	2.02	±45%	8.01	±87%
Ge	1.27	±13%	0.71	±35%	1.05	±30%	0.89	±48%	1.29	±5%	1.04	±17%	0.62	±67%	0.26	±42%	0.70	±64%
Rb*	25.21	±19%	2.68	±44%	16.26	±75%	15.41	±69%	25.89	±3%	24.47	±13%	8.31	±68%	2.56	±50%	12.38	±83%
Ba	779.83	±12%	800.85	±42%	788.18	±12%	581.62	±76%	767.73	±27%	1 834.96	±112%	2 307.72	±52%	1 614.16	±28%	1 599.42	±78%
Sr	327.85	±55%	794.31	±42%	513.23	±55%	330.43	±84%	258.53	±18%	542.01	±38%	1 143.26	±14%	1 146.34	±10%	827.30	±53%
Nb	7.11	±9%	4.78	±50%	6.18	±27%	5.02	±47%	6.83	±5%	5.70	±24%	3.22	±73%	4.03	±93%	4.56	±56%
Mo	2.20	±38%	8.77	±50%	4.81	±83%	4.04	±87%	1.47	±23%	1.01	±23%	1.14	±78%	1.68	±65%	1.70	±121%
Cd	0.37	±16%	0.52	±39%	0.43	±31%	0.40	±33%	0.28	±22%	0.54	±37%	0.38	±45%	0.29	±55%	0.37	±46%
In	0.06	±16%	0.03	±169%	0.05	±33%	0.04	±55%	0.06	±9%	0.05	±13%	0.02	±61%	0.01	±60%	0.03	±77%
Cs	1.64	±19%	0.17	±23%	1.05	±76%	1.00	±69%	1.68	±3%	1.59	±13%	0.54	±68%	0.17	±50%	0.81	±83%
Hf	2.86	±13%	1.16	±44%	2.18	±43%	1.58	±62%	2.31	±6%	1.92	±16%	0.82	±62%	0.58	±72%	1.22	±69%
Zr	98.25	±13%	42.02	±47%	75.76	±42%	56.36	±62%	86.95	±4%	73.12	±17%	32.68	±60%	23.77	±70%	46.61	±66%
Ta	0.48	±4%	0.33	±47%	0.42	±26%	0.32	±38%	0.40	±6%	0.39	±17%	0.30	±42%	0.31	±75%	0.33	±39%
W	0.37	±15%	0.09	±33%	0.26	±58%	0.30	±38%	0.38	±9%	0.37	±12%	0.23	±48%	0.15	±20%	0.26	±45%
Tl	0.21	±18%	0.11	±44%	0.17	±39%	0.23	±42%	0.15	±10%	0.28	±26%	0.14	±52%	0.08	±43%	0.16	±59%

to be continued

Continued form Table A3

	Hole U1381C						Hole U1414A											
	Unit I	RSD	Unit II	RSD	Bulk	RSD	Unit IA	RSD	Unit IB	RSD	Unit IIA	RSD	Unit IIB	RSD	Unit III	RSD	Bulk	RSD
Pb	6.44	±17%	2.68	±46%	4.93	±44%	4.37	±34%	5.23	±9%	5.72	±13%	4.13	±43%	2.46	±24%	4.06	±39%
Bi	0.07	±8%	0.04	±55%	0.06	±36%	0.06	±32%	0.07	±3%	0.09	±17%	0.07	±46%	0.03	±23%	0.06	±45%
Th	2.38	±33%	0.50	±36%	1.63	±70%	1.46	±68%	2.38	±17%	2.01	±26%	0.73	±53%	0.45	±70%	1.16	±78%
U	5.58	±22%	5.50	±47%	5.55	±25%	4.37	±18%	3.21	±22%	5.42	±26%	3.15	±44%	2.07	±36%	3.36	±44%
Sc	23.41	±32%	8.25	±60%	17.35	±57%	17.37	±62%	27.77	±5%	21.57	±18%	8.75	±60%	3.35	±23%	12.77	±79%
V	165.19	±16%	89.41	±45%	134.88	±34%	125.72	±44%	170.85	±5%	141.68	±18%	57.93	±65%	24.56	±32%	84.81	±73%
La	12.84	±14%	5.89	±45%	10.06	±39%	10.34	±29%	12.41	±9%	12.52	±6%	9.27	±41%	7.49	±45%	9.80	±34%
Ce	26.48	±9%	9.19	±49%	19.57	±48%	18.22	±47%	25.40	±8%	22.52	±17%	9.57	±54%	8.23	±80%	14.42	±60%
Pr	3.38	±10%	1.42	±46%	2.59	±42%	2.57	±39%	3.30	±8%	2.99	±11%	1.76	±46%	1.44	±54%	2.17	±45%
Nd	14.13	±9%	6.20	±48%	10.95	±40%	10.79	±38%	13.75	±7%	12.49	±9%	7.59	±47%	5.98	±50%	9.11	±44%
Sm	3.22	±10%	1.56	±46%	2.55	±37%	2.42	±39%	3.13	±6%	2.77	±7%	1.68	±47%	1.27	±49%	2.02	±46%
Eu	1.10	±7%	0.62	±39%	0.91	±29%	0.81	±44%	1.06	±5%	1.22	±41%	1.08	±44%	0.75	±20%	0.97	±41%
Gd	3.06	±10%	1.68	±45%	2.51	±32%	2.34	±35%	2.92	±5%	2.84	±11%	2.09	±49%	1.48	±41%	2.17	±40%
Tb	0.54	±13%	0.32	±35%	0.45	±30%	0.42	±32%	0.51	±6%	0.46	±6%	0.34	±50%	0.25	±40%	0.36	±40%
Dy	3.44	±13%	2.23	±45%	2.96	±27%	2.66	±30%	3.14	±6%	2.96	±8%	2.40	±49%	1.65	±34%	2.39	±38%
Ho	0.67	±14%	0.46	±37%	0.59	±25%	0.52	±25%	0.59	±6%	0.59	±12%	0.55	±49%	0.35	±29%	0.50	±37%
Er	1.95	±15%	1.37	±42%	1.72	±24%	1.54	±22%	1.72	±6%	1.75	±14%	1.74	±48%	1.09	±28%	1.52	±37%
Tm	0.31	±15%	0.22	±25%	0.27	±25%	0.25	±22%	0.27	±6%	0.28	±14%	0.28	±47%	0.17	±24%	0.24	±37%
Yb	1.85	±26%	1.56	±40%	1.73	±25%	1.60	±21%	1.76	±6%	1.80	±15%	1.81	±47%	1.09	±24%	1.56	±36%
Lu	0.30	±25%	0.25	±20%	0.28	±24%	0.26	±19%	0.28	±6%	0.30	±17%	0.31	±47%	0.18	±23%	0.26	±38%
Y	16.98	±24%	15.88	±45%	16.54	±22%	16.13	±14%	17.20	±8%	20.03	±19%	24.48	±45%	15.21	±22%	18.96	±39%

Note: *, the abundance of Rb is calculated from Rb/Cs content ratio which is about 15.4 in marine sediments (Plank and Langmuir, 1998); TFe_2O_3 represents total content of Fe_2O_3; RSD, relative standard deviation; –, no data.